Title

Integrated Maneuvering Control For Automated Highway Systems Based On A Magnetic Reference/sensing System

Authors

Tomizuka, Masayoshi
Hedrick, J. Karl
Pham, Hung

Publication Date

1995

CALIFORNIA PATH PROGRAM
INSTITUTE OF TRANSPORTATION STUDIES
UNIVERSITY OF CALIFORNIA, BERKELEY

Integrated Maneuvering Control for Automated Highway Systems based on a Magnetic Reference/Sensing System

Masayoshi Tomizuka
J. Karl Hedrick
Hung Pham

California PATH Research Report
UCB-ITS-PRR-95-12

This work was performed as part of the California PATH Program of the University of California, in cooperation with the State of California Business, Transportation, and Housing Agency, Department of Transportation; and the United States Department of Transportation, Federal Highway Administration.

April 1995

ISSN 1055-1425

Integrated Maneuvering Control for Automated Highway Systems based on a Magnetic Reference/Sensing System

Masayoshi Tomizuka
J. Karl Hedrick
Hung Pham

Partners for Advanced Transit and Highways (PATH)
Institute of Transportation Studies
University of California, Berkeley

November 1994

Abstract

In this report, a combined longitudinal and lateral eighteen-state vehicle chassis, engine, and drive train model is developed and validated against existing longitudinal-only and lateral-only vehicle models. The full-state model is simplified to a three-state model to facilitate controller design. The control task in a combined maneuver is defined as the simultaneous regulation of the vehicle's longitudinal and lateral spacings through application of throttle and steering. Two forms of a Sliding control law are derived based on the reduced order model. One version is decoupled in the longitudinal and lateral dynamics and forces, while the other retains the coupling terms. Nominal stability of the controllers is shown.

Comparisons are drawn among the lateral Frequency Shaped Linear Quadratic (FSLQ) and the coupled and decoupled Sliding controllers under the criteria of tracking, ride quality, and robust performance. The coupling effects under moderate to severe combined highway maneuvers are apparent. The coupled Sliding controller demonstrates quicker response and tighter tracking than does the decoupled form. In comparison to FSLQ, the Sliding formulation shows more consistent performance over the entire range of vehicle velocities. Robustness of the Sliding controller is shown against unknown wind disturbances and errors in vehicle mass estimates.

Table of Contents

Figures and Tables

1. Executive Summary

As the ever-present problem of freeway congestion becomes more acute, greater interest is being kindled on the subject of intelligent vehicles and highway systems (IVHS). It is believed that through automation, traffic flow can be made more efficient, thereby increasing highway volume throughput and relieving congestion. As one of the most active players in IVHS-related research in the past decade, the California Partners of Advanced Transit and Highways (PATH) Program has sponsored a number of projects that delve into the practical and engineering issues surrounding the implementation of such a system. Integral to this vision of IVHS is the successful realization of a functioning Advanced Vehicle Control Systems (AVCS).

Research groups at UC Berkeley have recently demonstrated the feasibility of AVCS with successful experiments involving vehicle longitudinal platooning and lateral road-following [8][13]. Specifically, the platooning tests require the vehicles to maintain a constant front-to-back spacing between successive vehicles during a series of longitudinal maneuvers. Lateral control in these tests is retained by the human driver. In the road-following experiments, steering is under automatic control, and the driver retains longitudinal control.

This report focuses on work done to build on the previous longitudinal and lateral results, and to merge the two control tasks into a single, comprehensive problem. It describes the efforts undertaken during the past year in the first phase of the project titled *Integrated Maneuvering Control for Automated Highway Systems Based on a Magnetic Reference/Sensing System.* Details of the vehicle modeling, control law development and computer simulation results are presented. The report is divided into four main parts as follows:

Chapter 2 documents the development of the vehicle simulation model. This model is derived from basic physical principles and accurately describes the behavior of

vehicle sprung mass, engine, drive train, and actuators in some detail. The model is subsequently used in computer simulations to validate and compare various control laws developed for combined vehicle control.

From this complete simulation model, a simple, reduced-order vehicle model (SVM) is derived in Chapter 3. The reduced model takes advantage of physical restrictions to eliminate a number of states and lessen the mathematical complexity. By reducing the model to a tractable form, the analysis of the system is greatly facilitated, and control law synthesis can more easily proceed.

Chapter 4 details the control law development. The control law is derived in two forms. One version of the law retains all of the dynamic coupling terms of the SVM -- particularly, the coupling associated with the tire tractive forces. The other version is predicated upon additional decoupling assumptions of the lateral and longitudinal dynamics of the SVM. An observer with preview information is incorporated into the control law in order to increase the ride quality performance.

Chapter 5 gives simulations results using the complete vehicle model. The control laws developed in Chapter 4 are compared against the lateral Frequency Shaped Linear Quadratic (FSLQ) control law [11] under the criteria of tracking, ride quality, and robust performance.

2. Vehicle Model

A mathematical model of a front-wheel driven, front-wheel steered automobile is developed for simulation. It consists of 18 states and describes the dynamics of the chassis, engine, tire, suspension, and steering and brake actuators in moderate fidelity. This model also includes characteristic maps of the engine and torque converter. There are no new experimental results presented in this section. Rather, this combined longitudinal/lateral package draws from the earlier results of the Ford and Toyota models [9][11]. As a consequence, its parameters retain a mix of the Towncar engine and Celica chassis data. While it is expected that the performance of this hybrid plant may not accurately reflect the behavior of either a Towncar or a Celica, its use in computer simulations for controller validation is justified. The reason is that variations in the plant parameters (as a reflection of the variations in the handling and power capabilities of different vehicles) are not critical as long as the values of these parameters are known to the controller. The contribution of this combined lateral and longitudinal simulation model is its presenting an accurate representation of the plant structure.

The states of the combined vehicle model are described by:

- x, V_x Longitudinal position, velocity
- y, V_y Lateral position, velocity
- z, V_z Vertical position, velocity
- $\psi, \dot{\psi}$ Yaw, yaw rate
- $\theta, \dot{\theta}$ Pitch, pitch rate
- $\phi, \dot{\phi}$ Roll, roll rate
- ω_{eng} Engine speed
- m_{air} Manifold air mass
- ω_{w_i} Speed of the i^{th} wheel; $i = 1,..,4$

while the inputs into the vehicle are given by:

- α Throttle angle
- T_{brake} Brake torque
- δ_f Front wheel steering angle

In addition to the vehicle dynamics, which we consider as the "plant dynamics," there are also the dynamics of the actuators. The actuator states are the plant inputs, while the actuator inputs are given by:

- α_C Commanded throttle angle
- $T_{brk\,C}$ Commanded brake torque
- δ_C Commanded front wheel steering angle

Other variables and parameters appearing in the model equations are:

β :	Vehicle side slip angle
χ :	Vehicle velocity angle
$C_{x(y)}$:	Longitudinal (lateral) wind drag coefficient
F_{roll} :	Rolling resistance of tires
h_2 :	Vertical distance from vehicle c.g. to roll center
$h_{4(5)}$:	Vertical (long.) distance from c.g. to pitch center
$\imath_s$:	Tire slip ratio
$I_{x\,(y)\,(z)}$:	Vehicle moment of inertia about -x (-y) (-z) axis
$l_{1(2)}$:	Longitudinal distance from c.g. to front (rear) axle
m :	Vehicle mass
$m_{air\ in\ (out)}$.	Mass of air entering (exiting) manifold
$M_{x(y)(z)}$:	Moment about -x (-y) (-z) axis
ν :	Tire slip angle
$s_{b1(b2)}$:	Track of front (rear) axle
T_{eng} :	Engine torque
T_{shaft}:	Drive shaft torque
T_{turb} :	Turbine torque
ω_{turb} :	Turbine speed
ζ_i :	Tire velocity angle
$F_{A_i(B_i)(P_i)}$	Net longitudinal (lateral) (normal) force on i^{th} tire
F_{damp_i} :	Damping force of i^{th} suspension joint
F_{spring_i} :	Spring force of i^{th} suspension joint
$F_{x_i(y_i)}$:	Traction force of i^{th} tire

A simple schematic of the vehicle model is provided on the following page. It describes the six degrees of freedom of the sprung mass as well as the relationship between the engine and drive train dynamics. The tires are numbered from left to right, beginning at the front.

Figure 2.1. Vehicle schematic.

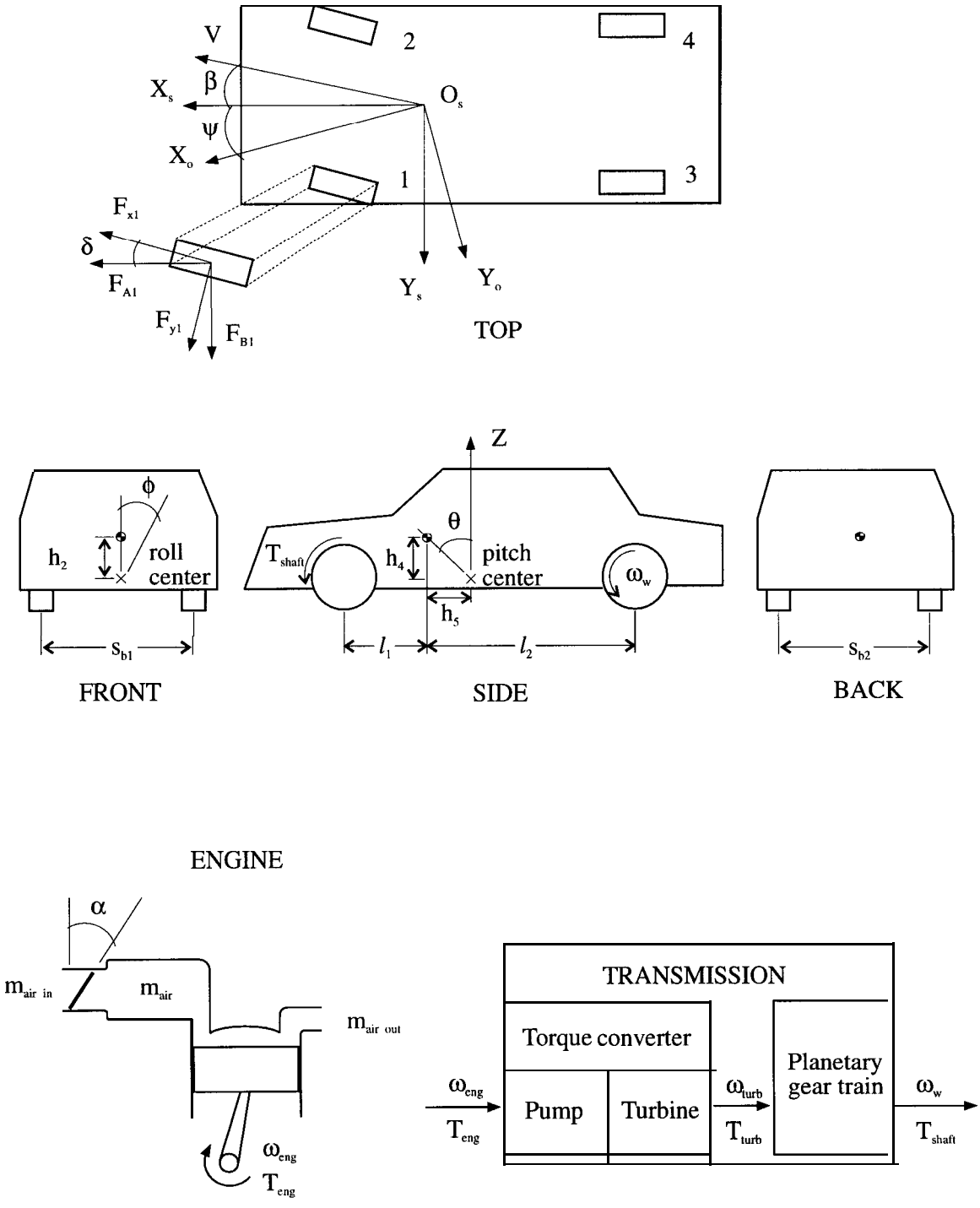

2.1 Sprung mass

Under the small angle assumption, the vehicle sprung mass equations of motion can be written as:

$$m[\dot{V}_x - V_y\dot{\psi} + h_4\ddot{\theta} + h_2\dot{\phi}\dot{\psi} + h_2\phi\ddot{\psi}] = \sum_{i=1}^{4} F_{A_i} - C_x V_x^2 - F_{roll} \quad 2.1$$

$$m[\dot{V}_y + V_x\dot{\psi} - h_2\ddot{\phi} + h_4\dot{\theta}\dot{\psi} + h_4\theta\ddot{\psi}] = \sum_{i=1}^{4} F_{B_i} - C_y V_y^2 \quad 2.2$$

$$m[\dot{V}_z + V_z\dot{\chi}\beta - h_5\ddot{\theta}] = \sum_{i=1}^{4} F_{P_i} - m\,g \quad 2.3$$

$$I_x[\ddot{\phi} - \theta\ddot{\psi} - \dot{\theta}\dot{\psi}] - (I_y - I_z)\dot{\theta}\dot{\psi} = M_x - \theta M_z \quad 2.4$$

$$I_y[\ddot{\theta} + \phi\ddot{\psi} + \dot{\phi}\dot{\psi}] - (I_z - I_x)\dot{\phi}\dot{\psi} = M_y + \phi M_z \quad 2.5$$

$$I_z[\ddot{\psi} + \theta\ddot{\phi} - \ddot{\theta}\phi] - (I_x - I_y)\dot{\theta}\dot{\phi} = M_z + \theta M_x - \phi M_y \quad 2.6$$

where the forces at each tire and the moments about center of mass are found from:

$$F_{A_i} = F_{x_i} - \delta_i * F_{y_i} \qquad i = 1,..,4 \quad 2.7$$

$$F_{B_i} = F_{y_i} - \delta_i * F_{x_i} \qquad i = 1,..,4 \quad 2.8$$

$$F_{P_i} = F_{spring_i} + F_{damp_i} \qquad i = 1,..,4 \quad 2.9$$

$$M_x = (\frac{S_{b1}}{2} + h_2\phi)F_{P_1} + (\frac{S_{b2}}{2} + h_2\phi)F_{P_3} - (\frac{S_{b1}}{2} - h_2\phi)F_{P_2} - (\frac{S_{b2}}{2} - h_2\phi)F_{P_4} - (z - h_5\theta)\sum_{i=1}^{4} F_{B_i} \quad 2.10$$

$$M_y = (l_2 + h_4\theta)(F_{P_3} + F_{P_4}) - (l_1 - h_4\theta)(F_{P_1} + F_{P_2}) - (z - h_5\theta)\sum_{i=1}^{4} F_{A_i} \quad 2.11$$

$$M_z = (l_1 - h_4\theta)(F_{B_1} + F_{B_2}) - (l_2 - h_4\theta)(F_{B_3} + F_{B_4}) - (\frac{S_{b1}}{2} + h_2\phi)F_{A_1} - (\frac{S_{b2}}{2} + h_2\phi)F_{A_3} + (\frac{S_{b1}}{2} - h_2\phi)F_{A_2} + (\frac{S_{b2}}{2} - h_2\phi)F_{A_4} \quad 2.12$$

2.2 Suspension

The suspension is modeled as four independent spring-dashpot systems [11]. That is, the spring and damper forces are completely determined by the local motion at each wheel location. The spring force contains a linear Hookean term and a fifth-order hardening term:

$$F_{spring_i} = C, \left(e_i + C_2 e_i^5\right) \qquad i = 1,..,4 \qquad 2.13$$

where the C_i's are spring constants and e_i is the suspension joint deflection at the i^{th} tire.

The damping force is obtained as a piece-wise linear function of the suspension deflection velocity.

$$F_{damp_i} = \begin{cases} D_{i_1} \dot{e}_i & \dot{e}_i < w \\ K_i + D_{i_2} (\dot{e}_i - w) & \dot{e}_i \geq w \\ -K_i + D_{i_2} (\dot{e}_i - w) & \dot{e}_i \leq w \end{cases} \qquad 2.14$$

where the D_i's, K_i's, and w are constants describing the damping characteristics [1 1].

2.3 Tire model

The traction and cornering forces are obtained from Bakker-Pacejka curve-fits of experimental data and are a function of the slip ratio (i_s), slip angle (v), and the tire normal force (F_P) [1]. The set of curves in Fig 2.2 represent fits based on tests from the Celica tires (Yokohama P205/60R1487H steel-belted radial) [12] under "ideal" laboratory conditions. The longitudinal curve-fits (Fig 2.2a) were obtained from traction-only experiments. Likewise, the lateral curve-fits (Fig 2.2b) were obtained from cornering-only tests. Deviations from ideal conditions are reflected in changes in the force-slip curves. The magnitude and shape of this change need to be determined by experimentation. However, in the absence of experimental data, a multiplicative effect on the ideal force-slip curves is currently assumed.

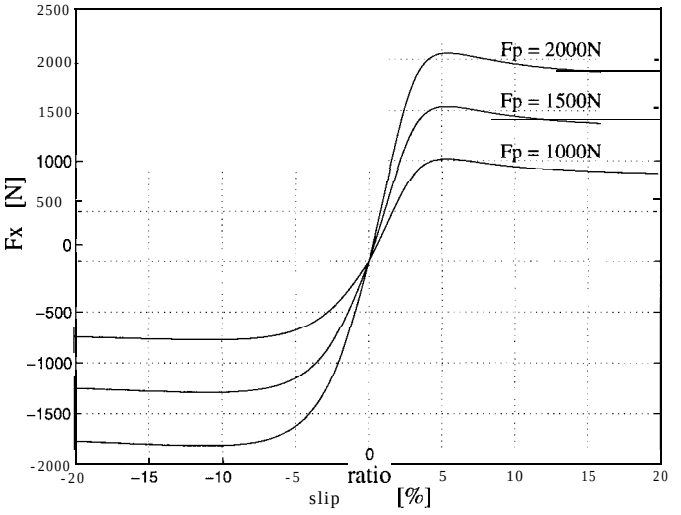

Figure 2.2a. Traction force (F,) curves as a function of slip ratio (i_s) and normal force (F_P).

braking $$i_s = \frac{V_x - r_w\omega_w}{V_x}$$

traction $$i_s = \frac{r_w\omega_w - V_x}{r_w\omega_w}$$

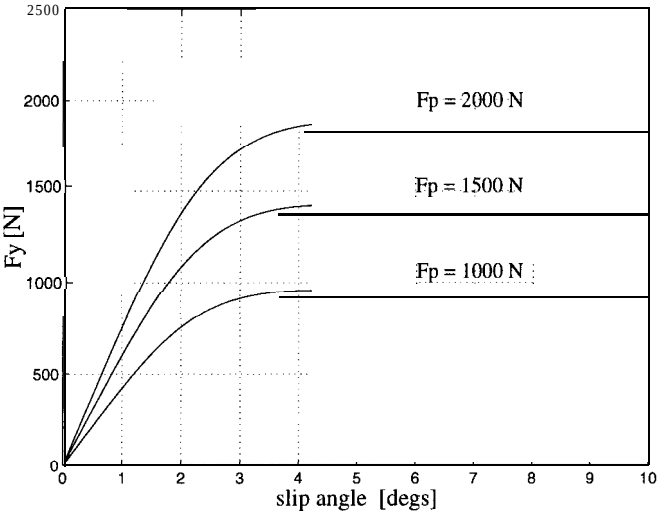

Figure 2.2b. Cornering force (F_y) curves as a function of slip angle (v) and normal force (F_P).

The i^{th} slip angle is defined as the angle between the i^{th} tire's orientation and its velocity vector. Its magnitude can be expressed as the difference between the tire's steering angle, δ_i, and its velocity angle, ζ_i ($\nu_i = \delta_i - \zeta_i$). Where, under small angle assumptions, this angle can be found from:

$$\zeta_1 = \frac{V_y + l_1\dot{\psi}}{V_x - \frac{s_{b1}}{2}\dot{\psi}}; \qquad \zeta_2 = \frac{V_y + l_1\dot{\psi}}{V_x + \frac{s_{b1}}{2}\dot{\psi}}$$

$$\zeta_3 = \frac{V_y - l_2\dot{\psi}}{V_x - \frac{s_{b2}}{2}\dot{\psi}}; \qquad \zeta_4 = \frac{V_y - l_2\dot{\psi}}{V_x + \frac{s_{b2}}{2}\dot{\psi}} \qquad 2.15$$

Note that for small values of v, the cornering force can be approximated as:

$$F_y \approx C_s \nu = C_s(\delta - \zeta) \qquad 2.16$$

where C_s, called the cornering stiffness, is the slope of the lateral force-slip curve and is defined by:

$$C_s = \frac{\partial}{\partial \nu} F_y(\nu)\Big|_{\nu=0} \qquad 2.17$$

The cornering stiffness is an important control parameter because it gives a direct relationship between the input, 6, and the lateral force, F_y. Unfortunately, it is also the most difficult parameter to measure as it depends on the normal force, tire camber angle, tire pressure and age, pavement material and weather conditions.

Again, we stress that the preceding curves are obtained from *traction-only* and *cornering-only* tests. For combined traction and cornering maneuvers, Bakker [1] proposed a modification of the tractive force equations by introducing a squared-norm correcting factor σ:

$$\sigma = \sqrt{\left(\frac{i_s}{i_{max}}\right)^2 + \left(\frac{\nu}{\nu_{max}}\right)^2} \qquad 2.18$$

where the terms, i_{max} and ν_{max}, refer to the values where the respective tractive forces are maximum. The combined forces are then modified by:

$$\bar{F}_x = \left(\frac{i_s}{i_{max}}\right)\left(\frac{1}{\sigma}\right) F_x \qquad 2.19$$

$$\bar{F}_y = \frac{\nu}{\nu_{max}} \frac{1}{\sigma} F_y \qquad 2.20$$

under the restrictions: $i_s < i_{max}$ and $\nu < \nu_{max}$. These restrictions should be checked in computer simulations under typical highway operating conditions.

2.4 Transmission and drive train

Balancing the moments about each wheel yields (Fig 2.4):

$$J_{w_i}\dot{\omega}_{w_i} = \frac{1}{2}T_{shaft} - \frac{3}{10}T_{brake} - r_{w_i}F_{x_i} \qquad i = 1,\ 2 \text{ (front)} \qquad 2.21a$$

$$J_{w_i}\dot{\omega}_{w_i} = -\frac{2}{10}T_{brake} - r_{w_i}F_{x_i} \qquad i = 3,\ 4 \text{ (rear)} \qquad 2.21b$$

where J_{w_i} is the polar moment of inertia of the i^{th} wheel, T_{brake} is the *total* available braking torque, and T_{shaft} is drive-shaft torque. This shaft torque is split evenly between the right and left driving wheels and reflects differential action. Similarly, the brake torque is also split evenly between the right and left wheels. However, the front/back distribution of T_{brake} follows a general "rule of thumb" 60/40 division.

Figure 2.3. Distribution of brake and drive torques.

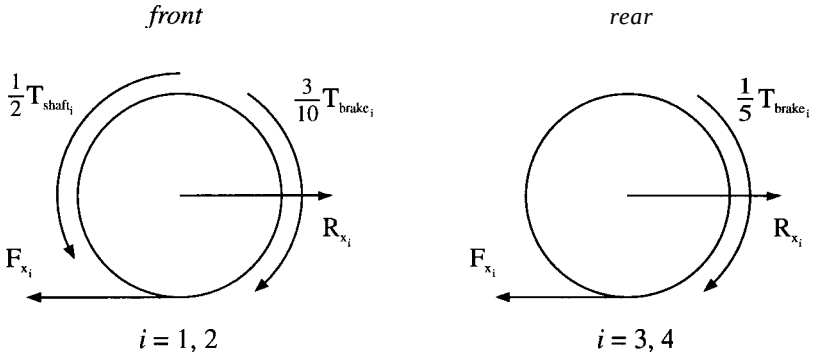

By neglecting the shaft and gear shift dynamics, the shaft torque can be taken as proportional to the torque converter output:

$$T_{turb} = r_{gear}r_{drive} * T_{shaft} \qquad 2.22$$

where r_{gear} and r_{drive} are the appropriate gear and drive ratios.

The afore-mentioned torque converter is a fluidic coupling between the engine and drive shaft, and acts to provide a smooth speed transmission during gear shifting operations. Consisting of a pump (input) and a turbine (output), the torque converter can act in either the *fluid* or *locked* modes. In the *fluid* mode, the input pump torque, T_{pump}, and output turbine torque, T_{turb}, are obtained from steady-state maps as a function of the speed ratio across the torque converter [9]:

$$T_{turb} = f_{map_1}\left(\frac{\omega_{turb}}{\omega_{eng}}, \omega_{eng}\right)$$

$$T_{pump} = f_{map_2}\left(\frac{\omega_{turb}}{\omega_{eng}}, \omega_{eng}\right) \qquad 2.23$$

where ω_{turb} is the turbine speed and ω_{eng} is the engine speed. In the *locked* position, the speeds and torques across the converter are matched (*i.e* $T_{pump} = T_{turb}; \omega_{pump} = \omega_{turb}$). In contrast, the engine and pump speeds are always matched ($\omega_{eng} \equiv \omega_{pump}$), regardless of mode of operation due to the pump's being attached directly to the engine.

Since gear shift dynamics are neglected, the turbine speed is simply related to the wheel speed by:

$$\omega_{turb} = \frac{1}{r_{gear} r_{drive}} \overline{\omega}_w \qquad 2.24$$

where $\overline{\omega}_w$ is the average speed of the front two wheels.

2.5 Engine

The engine dynamics are described by the 2-state model utilizing ω_{eng} and m_{air} [3]. Engine speed is governed by:

$$\dot{\omega}_{eng} = \frac{1}{J_{eng}}[T_{eng} - T_{pump}] \qquad 2.25$$

where J_{eng} is the engine polar moment of inertia, T_{eng} is the net engine torque, and T_{pump} is the pump torque coming from the torque converter. In this model, T_{eng} is obtained from steady-state maps as a function of engine speed and manifold pressure:

$$T_{eng} = f_{map}(\omega_{eng}, P_{man}) \quad \textbf{2.26}$$

Under constant temperatures and ideal gas conditions, P_{man} is calculated from the manifold air mass, m_{air}. In turn, this state is governed by the control volume equation:

$$\dot{m}_{air} = \dot{m}_{air\ in} - \dot{m}_{air\ out} \quad \textbf{2.27}$$

The second term on the right hand side of 2.27 ($\dot{m}_{air\ out}$) is obtained from maps similar to engine torque maps, while the first term is influenced by the throttle angle, a, according to:

$$\dot{m}_{air\ in} = \text{MAX}^* \ \text{PRI}(P_{man}) * \text{TC}(\alpha) \quad \textbf{2.28}$$

where MAX is an engine-specific constant indicating the maximum intake airflow, $\text{PRI}(\cdot)$ is the manifold pressure influence function, and $\text{TC}(\cdot)$ is the throttle characteristic function.

2.6 Actuators

The steering, brakes, and throttle actuators are three separate and radically different systems. While there has been some work in identification of the brake actuation system [5], the other actuator models are not completely understood. Nevertheless, as a rough approximation, it is assumed that all three can be approximated as first-order systems. Their approximate time constants and rate limits are shown in Table 2.1 below.

Table 2.1. Actuator parameters.

	time const [ms]	*max rate* [degs/s]
Brakes	75	---
Throttle	8	450
Steering	125	0.2

2.7 Model validation

The combined model is compared in open-loop simulations against the independent longitudinal and lateral vehicle simulation models. Their responses to different throttle and steering inputs and wind gust disturbances are plotted and qualitatively compared. It is seen that the results do agree in form, but differed slightly in quantitative terms. This is not surprising because the parameters of the combined model do not match completely with either of the independent models due to parameter overlap. For instance, each model had its own mass and tire characteristics. It is to be expected that with each set of those values, the vehicle should have different acceleration and cornering. Hence, if the combined model took one value each from the two models, its response should not be identical to either model, but should lie somewhere in between. A single vehicle data set is not used in the combined model because there are, currently, no one complete set of parameters available.

Due to its complexity, this model is not explicitly used for controller design. Instead, it is used to simulate the vehicle's response to various control laws. These simulation results give a good measure of the design, and allow the designer to make decisions regarding the relative merits of each control law before implementing the controller in actual field tests.

3. Simplified Vehicle Model (SVM)

The simulation model, while fully describing the dynamic behavior of the vehicle, is too complex for analysis and controller design. It is, therefore, necessary to make assumptions that will reduce the model to a tractable form, yet still capture the fundamental plant behavior. Simulations have revealed that the vertical, roll, and pitch motions can be neglected without any appreciable loss in accuracy. If we further assume a bicycle model, and if actuator and manifold dynamics are discounted, the plant can be reduced to the following three equations:

$$\dot{V}_x = -\frac{(r_w r^*)^2}{J^*}[C_x V_x^2 + F_{roll} - mV\dot{\psi}] + \frac{(r_w r^*)^2}{J^*}\left[\frac{1}{r_w r^*} T_{tot} - 2\delta_f F_{y_f}\right] \qquad 3.1$$

$$\dot{V}_y = -\frac{1}{m}[C_y V_y^2 - mV_x\dot{\psi} - 2(F_{y_l} + F_{y_r})] \qquad 3.2$$

$$\ddot{\psi} = \frac{2}{I_z}[l_1 F_{y_f} - l_2 F_{y_r}] \qquad 3.3$$

where J* and r* are the "effective" vehicle inertia and gear ratio, and T_{tot} is the net torque that the engine "sees".

$$J^* = (m\, r^2 + J_w)\left(r^*\right)^2 + J_{eng} \qquad 3.4$$

$$r^* = r_{drive} r_{gear} \qquad 3.5$$

$$Tot = T_{eng} - r^* T_{brake} \qquad 3.6$$

Note that in the above state equations, eqs 3.1-3, the wheel indices have been replaced by the subscripts, *f* (front) and *r* (rear).

Explicitly, the key assumptions used in the derivation of the simplified model are:

i) negligible roll and pitch motions
ii) no throttle, brake and steering actuator dynamics

iii) no engine manifold dynamics

iv) bicycle model *(i.e.* the dynamics of left and right sides are identical)

v) $V_x = \omega_w r_w$ (no slip condition)

vi) $T_{turb} = T_{pump}$ (locked torque converter)

vii) $C_s >> F_x$

The synthetic inputs into the simplified model are T_{tot} and F_{y_f}. They are synthetic in the sense that they are not the true inputs into the system, but can be directly obtained by proper choice of a, T_{brake}, and δ_f. Note that the reduced state equations are still nonlinear functions of the states. There is no attempt to linearize the system about an operating point. Instead, the term deletions result from a direct comparison of relative magnitudes over the entire vehicle operating range.

For convenience of notation, eqs 3.1-3 can be rewritten as:

$$\dot{V}_x = f_1 + k_1 T_{tot} - k_2 \delta_f F_{y_f} \qquad 3.7$$

$$\dot{V}_y = f_2 + k_3 F_{y_f} \qquad 3.8$$

$$\ddot{\psi} = f_3 + k_4 F_{y_f} \qquad 3.9$$

where f_1, f_2, f_3, and k_1, k_2, k_3, are the appropriately defined nonlinear functions and constants, respectively.

4.0 Control Development

The task of controlling a nonlinear system can be approached in a number of ways. A common technique is to first construct a linear approximation of the nonlinear system by taking a Jacobean expansion about the operating point. Then, the well developed tools of conventional linear controls can be applied to controller design. The main drawback to this approach is that the approximation is only valid *locally* around the operating point. If the operating range is large, or if the system is "highly nonlinear", it is necessary to linearize the plant about a number of operating points. Then, a separate linear controller can be designed for each linearized plant. As the system moves between operating points, the control gains are scheduled, or interpolated. This method, however, is computationally burdensome because of the need to compute many controllers off-line.

An alternative method, called state feedback linearization is to use state feedback to transform the original nonlinear system into an *equivalent* linear system. Thus, instead of approximating the system dynamics, feedback is used to cancel the nonlinearities directly. Then, a single controller can be designed for the equivalent system. Hence, consistent performance is achieved over a wide range of operating conditions without the need for intensive off-line computation and gain scheduling.

A control methodology which utilizes this state feedback linearization is Sliding control. Sliding control is a technique by which the original nonlinear n^{th}-order control problem is transformed into a stabilization problem in the scalar variable, S(x). This scalar is a linear function of the states and is defined so that the system input appears upon the first differentiation of S(x). The input can then be chosen to guarantee the convergence of S(x) to the surface, S(x) = 0. Once on the surface, the convergence of the states follows.

Sliding Control can be applied to the tracking problem, by defining a tracking error variable:

$$\tilde{y}(t) = y - y_d(t) \qquad 4.1$$

where y = h(x) is the system output and $y_d(t)$ is the desired trajectory. Define the desired error dynamics on the surface, S(x,t) = 0, as:

$$S(\mathbf{x},t) \equiv \left(\frac{d}{dt}+\lambda\right)^{r-1}\tilde{y} = \tilde{y}^{r-1} + (r-1)\lambda\tilde{y}^{r-2} + \ldots + \lambda^{r-1}\tilde{y} = 0 \qquad 4.2$$

where λ is a positive constant and *r* is the system relative degree, or number of differentiations of the output required to reach the system input. Notice that $\left(\frac{d}{dt}+\lambda\right)^{r-1}$ defines a Hurwitz polynomial of relative degree I, and a single differentiation of S will yield the control input. Then, the input, u, can be chosen so that

$$\dot{S}(\mathbf{x},t,u) = -\eta S \qquad 4.3$$

where η is a positive constant. This yields a stable first order differential equation for S which converges to the origin exponentially with rate η. Then, once "*on*" the surface S(x,t) = 0, the system error dynamics are defined by the Hurwitz polynomial in 4.2.

Hence, the Sliding control approach can be characterized as a two step pole-assignment approach where the first assignment of *r-1* poles is given by $(p + \lambda)^{r-1}$ and the second assignment is given by $(p + \eta)$. Here, the variable "p" is the Laplace variable.

The discussion thus far assumes that a u can be chosen in order to guarantee that $\dot{S}$ satisfies 4.3. This condition requires perfect knowledge of the plant. Suppose, however, that we know the plant only up to an additive term, *i.e.* $f_{true} = f_{nom} + \hat{f}$, where f_{true} is the true plant, f_{nom} is the nominal plant, and $\hat{f}$ is the plant error. Suppose, further, that the error term is bounded, $\|\hat{f}\| \le f_{max}$. Then, instead of 4.3, the best that can be expected is:

$$\dot{S} = -\eta S + \hat{f} \qquad 4.4$$

$$\Rightarrow \qquad |S(t)|_{t\to\infty} \le \frac{1}{\eta}\hat{f}_{max} \qquad 4.5$$

Consequently, asymptotic convergence of S can no longer be assumed. Instead, we can only guarantee that S be kept within a certain bound. Then, since the tracking error, $\tilde{y}$, is obtained from S through a stable *r-1*th order filter (or alternatively, a sequence of r-l first-order filters), *i. e.*

$$\tilde{Y}(p) = \frac{1}{(p+\lambda)^{r-1}} S(p) \qquad 4.6$$

$$\Rightarrow \qquad |\tilde{y}(t)|_{t\to\infty} \le \frac{1}{\lambda^{r-1}} |S(t)|_{t\to\infty}.$$

Thus, the bounds on S are reflected in the bounds on $\tilde{y}$.

Fortunately, it happens that in many instances, $\hat{f}$ is constant or is slowly time-varying. In this case, we can add integral action to drive the tracking error to zero. Instead of defining S as in 4.2, we write:

$$S = \left(\frac{d}{dt} + \lambda\right)^r \int_0^t \tilde{y} dt \qquad 4.7$$

Note that the dynamic equation for S still has relative degree *1* since the relative degree of $\int \tilde{y} dt$ is *r+1*. Then, for $\hat{f} = K_{const}$,

$$|S(t)|_{t\to\infty} = \frac{1}{\eta} K_{const} \qquad 4.8$$

and S converges to a surface defined by a constant. Once on the surface, the integral of error converges to

$$\Rightarrow \qquad \int_0^\infty \tilde{y} dt = \frac{1}{\lambda^r \eta} K_{const} \qquad 4.9$$

Then, from the convergence of the integral and uniform continuity condition on $\tilde{y}$, we get that $\tilde{y}$ converges to the origin. The uniform continuity of $\tilde{y}$ stems from the physical restrictions on the system and desired trajectory. The integral action provides an additional benefit when the initial error is large by smoothing the transient.

4.1 Vehicle Control

4.1.1 outputs

The system's outputs are defined as the longitudinal spacing error and the lateral error from road center. Figure 4.1 shows the output configuration of the proposed experimental setup.

Figure 4.1. Diagram of two vehicle system.

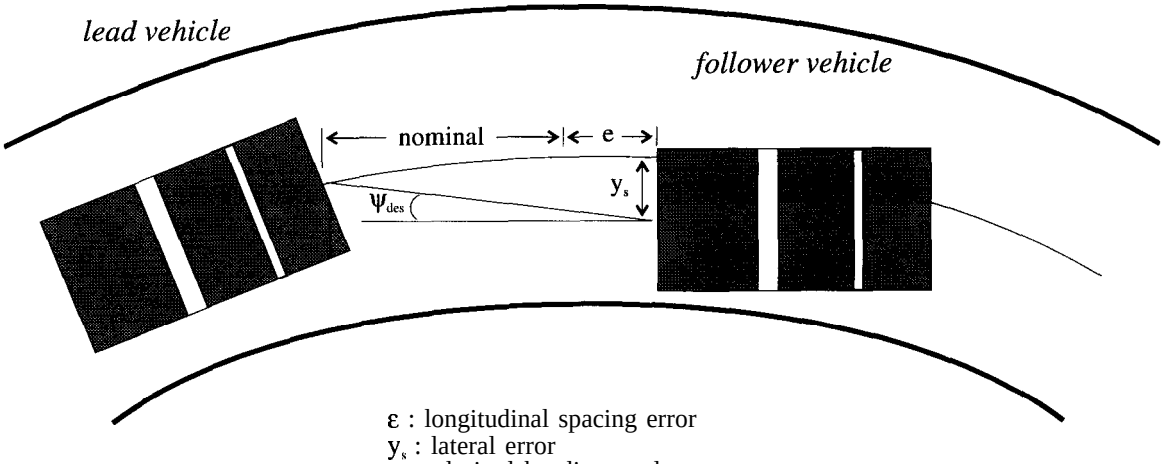

Mathematically, the longitudinal error is:

$$\varepsilon = x_{car} - x_{lead} + space_{nom} \qquad 4.10$$

where x_{car} is the longitudinal position of the vehicle, x_{lead} is the preceding vehicle's position, and $space_{nom}$ is the nominal intercar spacing. The kinematics of the lateral sensor are given by:

$$\dot{y}_s = V_y + V_x(\psi - \psi_{rd}) + d_s(\dot{\psi} - \dot{\psi}_{rd}) \qquad 4.11$$

where ψ_{rd} is the road (or desired) yaw angle, and d_s is the longitudinal distance from magnetometer to vehicle c.g.

For the vehicle control problem, we are interested in the simultaneous regulation of ε and y,, through the application of the throttle, a, and steering, δ_f. Braking is not considered in the present phase of the control development. We now have a two-input, two-output control problem. The extension of single-input, single-output Sliding control to multiple-input, multiple-output systems can be made by defining a separate scalar variable, S_i for each output, y_i. Then, the inputs can be chosen so that the exponential decays of the S_i's are simultaneously guaranteed in the absence of uncertainties.

Then, there is the question of how much coupling exists between the lateral and longitudinal dynamics during a combined maneuver. Unfortunately, it is difficult to obtain a definitive answer because the degree of coupling depends on a number of factors, such as type and severity of maneuvers, and road and tire conditions. Therefore, two solutions to the combined control problem are presented. One solution stresses some additional decoupling assumptions to the SVM, while the other concentrates on an integrated approach to controller design.

4.1.2 Decoupled control

In the decoupled controller design, two additional approximations of the simplified model and output equations are made from the outset:

$$\dot{V}_x \approx f_1 + k_1 T_{tot} \tag{4.12}$$

$$\ddot{y}_s \approx \dot{V}_y + V_x\dot{\tilde{\psi}} + d_s\ddot{\tilde{\psi}} \tag{4.13}$$

In words, we assume that the longitudinal acceleration is not affected by the lateral tire force and that the car's forward speed can be treated as a parameter in lateral control.

To obtain the control surfaces, define:

$$\begin{bmatrix} S_1 \\ S_2 \end{bmatrix} = \begin{bmatrix} (\frac{d}{dt}+\lambda_1)^2 & (\frac{d}{dt}+\lambda_2)^2 \end{bmatrix} \begin{bmatrix} \int_0^t \varepsilon dt \\ \int_0^t y_s dt \end{bmatrix} \tag{4.14}$$

Differentiating this expression yields:

$$\frac{d}{dt}\begin{bmatrix} S_1 \\ S_2 \end{bmatrix} = \begin{bmatrix} \ddot{\varepsilon} + 2\lambda_1\dot{\varepsilon} + \lambda_1^2\varepsilon \\ \ddot{y}_s + 2\lambda_2\dot{y}_s + \lambda_2^2 y_s \end{bmatrix} \tag{4.15}$$

$$\Rightarrow \quad \frac{d}{dt}\begin{bmatrix} S_1 \\ S_2 \end{bmatrix} = \begin{bmatrix} V_x - a_{lead} + 2\lambda_1\dot{\varepsilon} + \lambda_1^2\varepsilon \\ \dot{V}_y + V_x\dot{\tilde{\psi}} + d_s\ddot{\tilde{\psi}} + 2\lambda_2\dot{y}_s + \lambda_2^2 y_s \end{bmatrix}$$

Substituting in the decoupled state equations leads to:

$$\frac{d}{dt}\begin{bmatrix} S_1 \\ S_2 \end{bmatrix} = \begin{bmatrix} f_1 - a_{lead} + 2\lambda_1\dot{\varepsilon} + \lambda_1^2\varepsilon \\ f_2 + V_x\dot{\tilde{\psi}} + d_s(f_3 - \ddot{\psi}_{rd}) + 2\lambda_2\dot{y}_s + \lambda_2^2 y_s \end{bmatrix} + \begin{bmatrix} k_1 T_{tot} \\ k_3 F_{y_f} + d_s k_4 F_{y_f} \end{bmatrix} \tag{4.16}$$

By inspection, it is seen that 4.16 is decoupled in the synthetic controls, T_{tot} and F_{y_f}. Hence, it is a simple matter to choose the synthetic inputs, $T_{tot\,des}$ and $F_{y_f\,des}$, so

that condition 4.3 is satisfied for both S_1 and S_2 in the absence of uncertainties. Choose the inputs to be:

$$T_{tot\ des} = -\frac{1}{k_1}[f_1 - a_{lead} + 2\lambda_1\dot{\varepsilon} + \lambda_1^2\varepsilon + \eta_1 S_1] \qquad 4.17$$

$$F_{y_f\ des} = -\frac{1}{(k_3 + d_s k_4)}[f_2 + V_x\dot{\tilde{\psi}} + d_s(f_3 - \ddot{\psi}_{rd}) + 2\lambda_2\dot{y}_s + \lambda_2^2 y_s + \eta_2 S_2]$$

Then, in the presence of constant uncertainties, we get:

$$\begin{bmatrix}\dot{S}_1\\ \dot{S}_2\end{bmatrix} = \begin{bmatrix}-\eta_1 S_1 + \frac{1}{k_1}\hat{d}_1\\ -\eta_2 S_2 + \frac{1}{(k_2 + d_s k_3)}\hat{d}_2\end{bmatrix} \qquad 4.18$$

$$\Rightarrow \quad \left\|\begin{bmatrix}S_1\\ S_2\end{bmatrix}\right\|_{t\to\infty} = \begin{bmatrix}\frac{1}{\eta_1 k_1}\hat{d}_1\\ \frac{1}{\eta_2(k_2 + d_s k_3)}\hat{d}_2\end{bmatrix}$$

$$\Rightarrow \quad \left\|\begin{bmatrix}\int_0^\infty \varepsilon dt\\ \int_0^\infty y_s dt\end{bmatrix}\right\| = \begin{bmatrix}\frac{1}{\lambda_1^2\eta_1 k_1}\hat{d}_1\\ \frac{1}{\lambda_2^2\eta_2(k_2 + d_s k_3)}\hat{d}_2\end{bmatrix}$$

$$\Rightarrow \quad \begin{bmatrix}\varepsilon\\ y_s\end{bmatrix}_{t\to\infty} = \begin{bmatrix}0\\ 0\end{bmatrix}$$

and asymptotically perfect tracking is achieved.

From the synthetic $T_{tot\ des}$ and $F_{y_f\ des}$, the real controls can be obtained. The desired throttle angle, α_{des}, can be referenced from a look-up table based on the engine speed, ω_{eng}, and desired engine torque, $T_{eng\ des} = T_{tot\ des}$. The desired steering angle is found through the relation:

$$\delta_{f\ des} = \frac{1}{C_{s_f}}F_{y_f\ des} - \zeta_f \qquad 4.19$$

4.1.3 Couvled control

If the decoupling assumptions of the SVM are not made, the longitudinal and lateral dynamics become coupled in the control. The cross-effects of the inputs on vehicle motion in both the -x and -y directions are now assumed to be non-negligible. Under this premise, the developed control laws become more complicated, with the added terms reflecting the coupling dynamics.

Using the same surface definitions as before, but noting that the magnetometer's lateral acceleration is now $\ddot{y}_s = \dot{V}_y + \dot{V}_x\tilde{\psi} + V_x\dot{\tilde{\psi}} + d_s\ddot{\tilde{\psi}}$, we obtain:

$$\frac{d}{dt}\begin{bmatrix} S_1 \\ S_2 \end{bmatrix} = \begin{bmatrix} V_x - a_{lead} + 2\lambda_1\dot{\varepsilon} + \lambda_1^2\varepsilon \\ \dot{V}_y + \dot{V}_x\tilde{\psi} + V_x\dot{\tilde{\psi}} + d_s\ddot{\tilde{\psi}} + 2\lambda_2\dot{y}_s + \lambda_2^2 y_{s_I} \end{bmatrix} \qquad 4.20$$

$$\frac{d}{dt}\begin{bmatrix} S_1 \\ S_2 \end{bmatrix} = \begin{bmatrix} f_1 - a_{lead} + 2\lambda_1\dot{\varepsilon} + \lambda_1^2\varepsilon \\ f_2 + f_1\tilde{\psi} + V_x\dot{\tilde{\psi}} + d_s(f_3 - \ddot{\psi}_{rd}) + 2\lambda_2\dot{y}_s + \lambda_2^2 y_s \end{bmatrix}$$

$\Rightarrow$

$$+ \begin{bmatrix} k_1 T_{tot} - k_2\delta_f F_{y_f} \\ k_3 F_{y_f} + (k_1 T_{tot} - k_2\delta_f F_{y_f})\tilde{\psi} + d_s k_4 F_{y_f} \end{bmatrix}$$

The surface attraction equations are now quadratic and coupled in the steering and torques.

In order to avoid solving for the squared terms, we define an equivalent control:

$$u_{eq} = k_1 T_{tot} - k_2\delta_f F_{y_f} \qquad 4.21$$

$$\frac{d}{dt}\begin{bmatrix} S_1 \\ S_2 \end{bmatrix} = \begin{bmatrix} f_1 - a_{lead} + 2\lambda_1\dot{\varepsilon} + \lambda_1^2\varepsilon \\ f_2 + f_1\tilde{\psi} + V_x\dot{\tilde{\psi}} + d_s(f_3 - \ddot{\psi}_{rd}) + 2\lambda_2\dot{y}_s + \lambda_2^2 y_s \end{bmatrix}$$

$\Rightarrow$

$$+ \begin{bmatrix} k_3 F_{y_f} + u_{eq} + u_{eq}\tilde{\psi} + d_s k_4 F_{y_f} \end{bmatrix}$$

The change of variable has the effect of decoupling the surface equations. The inputs can be chose as:

$$u_{eq\ des} = -[f_1 - a_{lead} + 2\lambda_1\dot{\varepsilon} + \lambda_1^2\varepsilon + \eta_1 S_1] \qquad \textbf{4.22}$$

$$F_{y_f\ des} = -\frac{1}{(k_3 + d_s k_4)}[f_2 + V_x\dot{\tilde{\psi}} + d_s(f_3 - \ddot{\psi}_{rd}) + 2\lambda_2\dot{y}_s + \lambda_2^2 y_s + \eta_2 S_2 + (a_{lead} - 2\lambda_1\dot{\varepsilon} - \lambda_1^2\varepsilon - \eta_1 S_1)\tilde{\psi}]$$

Recall that in a combined maneuver, the cornering force equations are modified by:

$$\bar{F}_y = \frac{v}{v_{max}\sigma} * F_y$$

We make use of this force modification in the control to give a more accurate steering command during a combined maneuver. For practical purposes, however, it is very difficult to get an accurate estimate of the slip, i_s, and hence σ. However, if we assume isotropic behavior of the tires, then the above equation can be reduced to:

$$\bar{F}_y = \frac{F_y}{F_{tot}} * F_y \qquad \textbf{4.23}$$

where $F_y = C_s(\delta - \zeta)$ is the nominal cornering force, and $F_{tot} = \sqrt{F_x^2 + F_y^2}$ is the net resultant force (Fig 4.2).

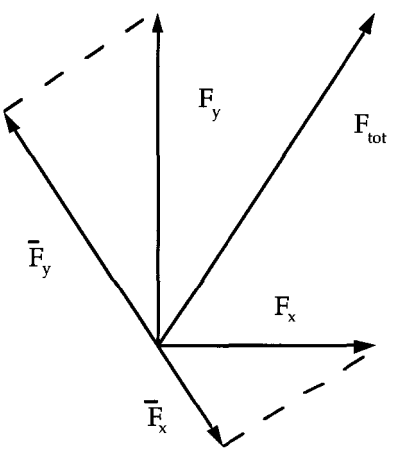

Figure 4.2. Geometric interpretation of the modified tractive forces.

By introducing the concept of a modified cornering stiffness, C_s^*, the cornering force can be expressed as:

$$\bar{F}_y = C_s^*(\delta - \zeta) \qquad 4.24$$

Making use of the above definition, and noting that $F_{tot} = |\bar{F}_y| + |\bar{F}_x|$, C_s^* can be approximated from:

$$C_s^* \nu = \frac{C_s \nu}{(|C_s^* \nu| + |\bar{F}_x|)} * C_s \nu \qquad |\nu| > 0 \qquad 4.25$$

$$\Rightarrow \quad C_s^{*2}|\nu| + C_s^*|\bar{F}_x| - C_s^2 \nu = 0$$

$$\Rightarrow \quad C_s^* \approx \frac{-|\bar{F}_x| + \sqrt{\bar{F}_x^2 + 4(C_s \nu_{old})^2}}{2|\nu_{old}|}$$

where the traction force, $\bar{F}_x$ is calculated from:

front: $$F_{x_f} = \frac{1}{2r_w^2 r^{*2}}[r_w r^* T_{eng} - \dot{V}_x(J_{eng} + 2J_w r^{*2})] \qquad 4.26$$

rear: $$F_{x_r} = \frac{-1}{2r_w^2 r^{*2}}[2\dot{V}_x J_w r^{*2}]$$

Utilizing the modified cornering stiffness, the desired steering angle is found to be:

$$\delta_{fdes} = -\frac{1}{C_{s_f}^*(k_3 + d_s k_4)}[f_2 + V_x \ddot{\tilde{\psi}} + d_s(f_3 - \ddot{\psi}_{rd}) + 2\lambda_2 \dot{y}_s + \lambda_2^2 y_s + \eta_2 S_2 + (a_{lead} - 2\lambda_1 \dot{\varepsilon} - \lambda_1^2 \varepsilon - \eta_1 S_1)\tilde{\psi}] + \zeta_f \qquad 4.27$$

Then, from δ_{des} and the equivalent control, $u_{eq\ des}$, the desired torque can be found:

$$T_{tot\ des} = \frac{1}{k_1}[u_{eq\ des} + k_2 \delta_{f\ des} F_{y_f\ des}] \qquad 4.28$$

The coupling effects are apparent in the tractive forces and cross-products of longitudinal and yaw errors. However, the question of how big a role the coupling terms play in computing the control effort cannot be readily answered. Certainly, bounds can be placed on the states and outputs. But while their relative magnitudes can be compared, their relative contribution to controller performance, in a given maneuver, is more difficult to quantify. A more holistic approach, such as a direct simulations comparison, is detailed in the next chapter.

4.1.4 Controller implementation

In order to implement the control law, information on all states of the SVM is needed. The longitudinal velocity (V,) is estimated from wheel speed measurements. These measurements are relatively clean but may give offset errors in the estimate due to inexactly known wheel radius and slip. The yaw rate ($\dot{\psi}$) is measured with a yaw rate sensor. The lateral velocity (V,) is obtained from integrating the estimate of the lateral acceleration with respect to the body-fixed coordinates ($\dot{V}_y$). This quantity can be calculated from lateral accelerometer measurements, $\ddot{y}_{accel}$:

$$\dot{V}_y = \ddot{y}_{accel} - r_w \omega_w \dot{\psi} \qquad 4.29$$

However, this method of estimating V_y suffers from both offset error and noisy sensor measurements. At present, these state measurements are all assumed to be available.

The parameters utilized to compute the control effort may deviate substantially from the nominal values. In particular, the estimates of mass, wind drag coefficient and cornering stiffness are especially prone to fluctuations. Thus, the effects of the parameter errors on the controller performance will also be investigated in simulation.

Another important consideration is how the disturbance information is obtained. Presently, the longitudinal disturbance (lead vehicle velocity and acceleration) is radioed from the preceding car at regular intervals. The transmission is synchronized with the controller update, and thus, presents little problem from the timing standpoint. On the other hand, the lateral error and road curvature information are received from the magnetic markers imbedded in the road. The frequency of these updates, which depend on vehicle speed and marker spacing, do not coincide with the controller frequency. A further complication stems from sudden step changes in road geometry. Often, the road may change direction or increase curvature abruptly. These factors tend to excite the controller to unnecessarily high activity and can lead to undesirable dynamic behavior and decreased ride quality.

Thus, instead of relying purely on the discrete sensor readings, the controller could be made to minimize a *model* of the lateral error, $\hat{y}_s$, based on the measured error, the present and future curvature information, and the vehicle states. This estimate can be obtained from a simple 1 -state Luenberger observer of the form:

$$\dot{\hat{y}}_s = V_y + V_x(\psi - \psi_{des}) + d_s(\dot{\psi} - \dot{\psi}_{des}) + L(y_{sQ} - \hat{y}_s) \qquad 4.30$$

where L is the observer gain, y_{sQ} is the measured lateral error, and ψ_{des} and $\dot{\psi}_{des}$ are the desired *model* yaw and yaw rate:

$$\dot{\psi}_{des} = \frac{V_x}{\rho_{model}} \qquad 4.31$$

The measured lateral error, y_{sQ}, is updated upon encountering a marker. In between marker readings, y_{sQ} is held constant in the observer equation (4.30). Other types of observers will be investigated in the future to determine the best performance.

The motivation for using the modeled radius, ρ_{model}, as opposed to the true radius, is to provide a smooth transition between curves. As mentioned earlier, the changes in

curvature are abrupt and discontinuous. However, by making use of a ρ_{model} as reference, we can better control the dynamics of the disturbance, thereby insuring the continuity of $\hat{y}_s$ and the control signal.

The model-generated radius is obtained from passing a previewed segment of the road curvature through a shaping filter, h(t):

$$\frac{1}{\rho_{model}}(t) = \int_{tt}^{t+t_p} \frac{1}{\rho}(t)h(t-\tau)d\tau \qquad 4.32$$

where t_p is the preview segment.

Figure 4.3. Curvature model.

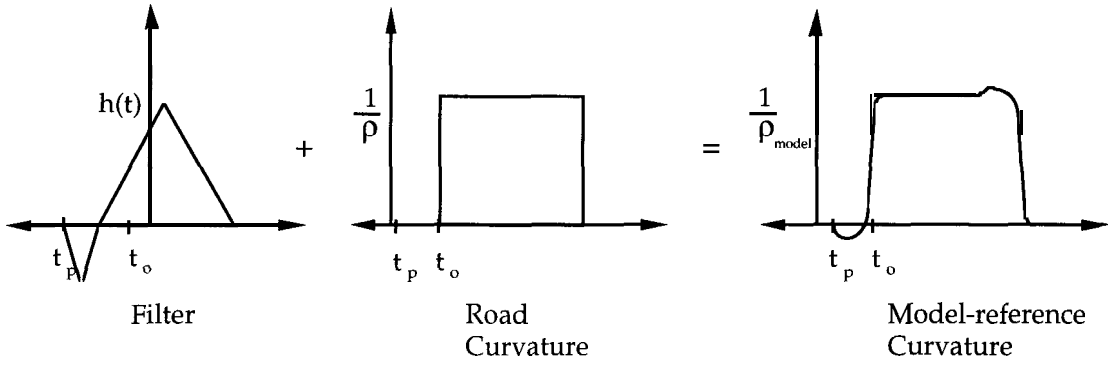

Define the curvature error as:

$$\varepsilon_\rho(t) = \frac{1}{\rho}(t) - \frac{1}{\rho_{model}}(t) \qquad 4.33$$

Observe that this error is a function of both the preview length and the shaping filter parameters (Fig 4.3). Since ride quality is an important consideration, we want to

minimize the rate of change of ρ_{model}. However, this tendency competes directly with the minimization of ε_ρ, and hence, the minimization of the observer error, $\varepsilon_{y_s} = y_s - \hat{y}_s$.

Therefore, it is required that the filter parameters and preview segment be selected so as to give the maximum trade-off between ride quality and observer error. Unfortunately, it is difficult to obtain a closed-form analytical solution because ε_{y_s} depends also on the observer gain and the vehicle states. Consequently, a parametrization study was conducted in order to obtain the "optimal" preview time and filter coefficients. The simulations revealed the following set of parameters for the curvature shaping filter.

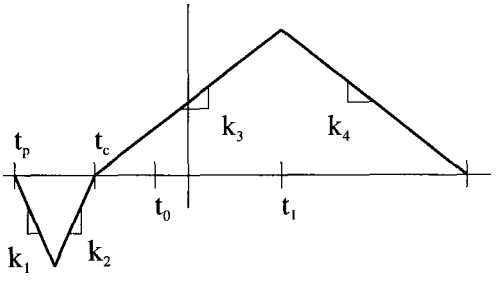

to = 0s
t_p = -0.8s
t_c = -0.27s
t_1 = 0.91s
k_1 = 0.74/s
k_2 = -0.74/s
k_3 = 1.17/s
k_4 = -1.17/s

5. Computer Simulations

The complete vehicle simulation model is used to compare the performances of the coupled and decoupled Sliding controllers under a number of different highway scenarios. In addition, the study also includes comparisons between Sliding and the previously wrought lateral FSLQ controller [13]. The comparison is based on the following four criteria: 1) tracking, 2) passenger comfort, 3) insensitivity to environmental disturbances, and 4) robustness to parameter errors. Again, it should be noted that only throttle and steering control are considered. Braking is not included in the study.

5.1 Nominal performance

A number of trials are conducted with accelerations and road curvatures of varying magnitudes. The longitudinal accelerations ranged from [-0.05g, 0.15g], while the lateral accelerations are varied from [Og, 0.3g]. The tests simulated cornering-only, traction-only, and combined maneuvers. The simulations revealed that the coupling due to the kinematics terms are minor under "normal" highway operations, but that the coupling between the tractive forces are significant. Under moderate maneuvers, the degree of coupling is 20-30% (as measured by the reduction in the cornering stiffness). Under more severe maneuvers, the figure approaches 50%. Correspondingly, there is an increase in the tracking performance of the coupled controller over that of the decoupled form. The margin of improvement varies according to severity and type of maneuvers. It is seen that, typically, the greatest improvements occurred in maneuvers wherein the vehicle accelerates during the middle of a turn.

The constant velocity comparisons between the lateral Sliding and FSLQ controllers revealed minor advantages of the Sliding control in terms of tracking and ride quality. However, this may be attributed to the fact that the FSLQ gains used in the simulations had been tuned previously for the Toyota vehicle (the parameters of the

simulation vehicle are not matched exactly with the Toyota). Hence, the FSLQ performance obtained in these simulations may not be "optimal." More telling, however, are the comparisons made under combined maneuvers. Since the FSLQ controller is derived from a linearized plant, it should be expected that quick changes in the velocity (or operating point) will degrade controller performance. Simulations conducted with large accelerations did indicate a degradation in the tracking performance of the FSLQ controller. In contrast, the Sliding control exhibited fairly consistent performance over a wide range of velocities and accelerations. It is also emphasized that the gains chosen for the Sliding control are obtained without extensive off-line computations. Rather, the gains are chosen directly by pole placement with minimal tuning. The set of gains chosen for this study is: $\eta_1 = 1.0$, $\eta_2 = 2.8$, $\lambda_1 = 0.6$, $\lambda_2 = 1.2$.

coupled vs. decoupled

A comparison of the two Sliding controllers are presented for a sample trial. A sketch of the test profile is shown in Fig 5.1 below. The road profile consists of a single curve of radius, $\rho = 140$m. The vehicle is commanded to accelerate from 20m/s (45mph) to 24m/s (54mph) beginning at the midpoint of the curve. This corresponds to a maximum commanded longitudinal acceleration of $\dot{V}_{lead} = 0.4\text{m/s}^2$, and a maximum total lateral acceleration of 3.5m/s^2.

Figure 5.1. Commanded vehicle velocity and road curvature, I.

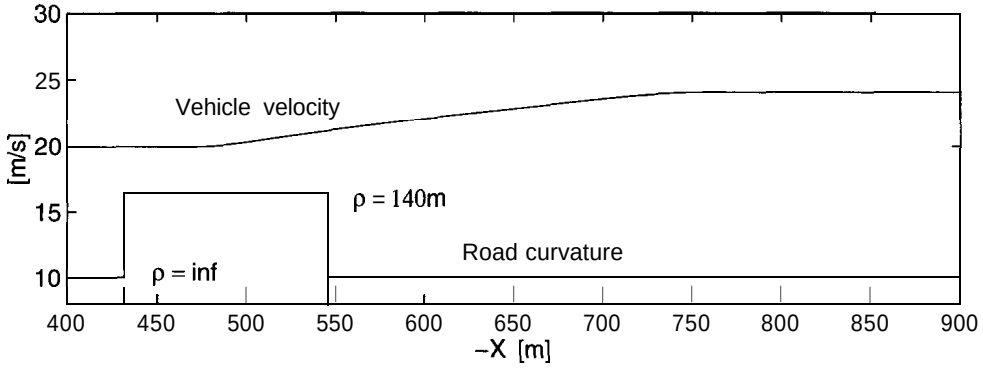

The throttle inputs of the two controllers are plotted in Fig 5.2. Note the increase in the throttle command at X = 430m corresponding to the onset of curve. The coupling is apparent in the increased demand for power during the curved section despite the velocity's being constant. Note, also, the drop-off in throttle at X = 540m corresponding to the end of curve. The differences between the coupled and controls are most apparent at these two critical points, where it is seen that the decoupled input lags the coupled input.

Figure 5.2. Comparison of throttle inputs, coupled vs. decoupled control.

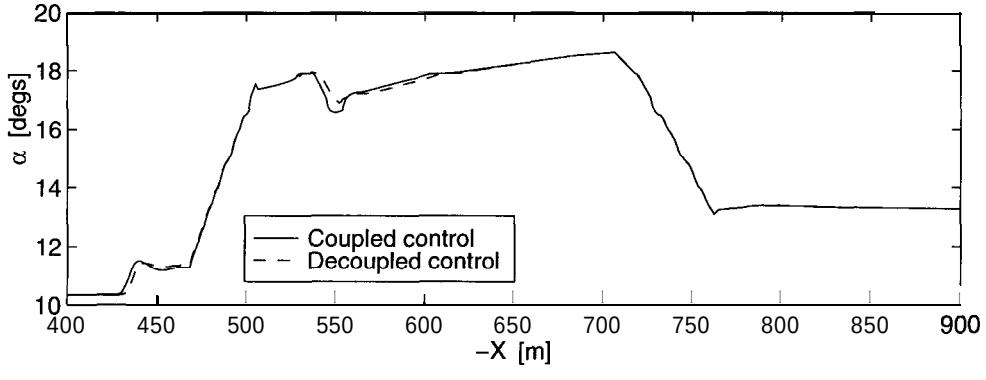

The plot of the longitudinal spacing errors is shown in Fig 5.3. As indicated in the previous plot, the decoupled controller is more sluggish, and the result is that the vehicle begins to drop off relative to its desired spacing (negative error) at the beginning of the curve. Conversely, the coupled controller adequately compensates for the coupling forces and the error remains close to zero. Then, as the vehicle exits the curve (X = 540m), the decoupled error overshoots; whereas, the coupled controller again provides adequate compensation.

Figure 5.3. Longitudinal tracking errors of coupled and decoupled control.

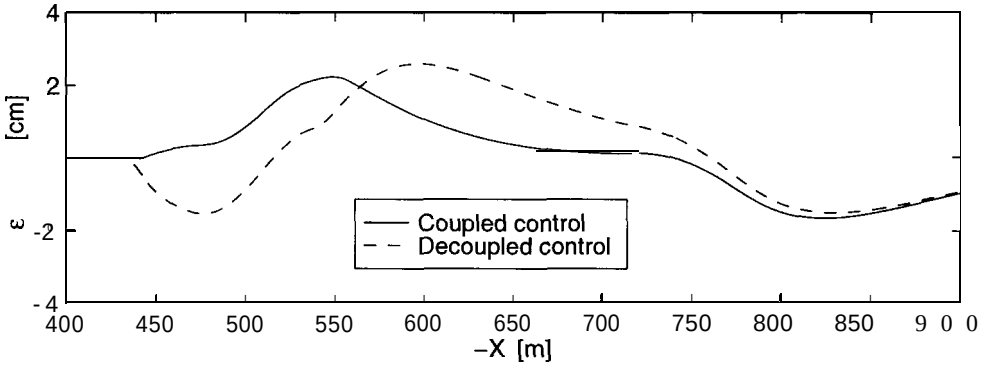

As a measure of the passenger comfort level, the longitudinal jerks are plotted in Fig 5.4 below. It is seen that the jerks are reasonable for both controls -- being well within the generally acceptable $2 m/s^3$ limits. These jerks are a strong function of the particular choice of gains used in Sliding control. As a consequence, it is possible to shape the jerk response directly by proper choice of gains. This tendency, however, competes directly with the tracking demands, and it becomes an engineering judgment in determining the acceptable trade-offs between passenger comfort and tracking performance. As a possible direction for future research, we could formalize the performance trade-offs and investigate this problem within an LQ optimization framework.

Figure 5.4. Longitudinal ride comfort performance of Sliding controllers.

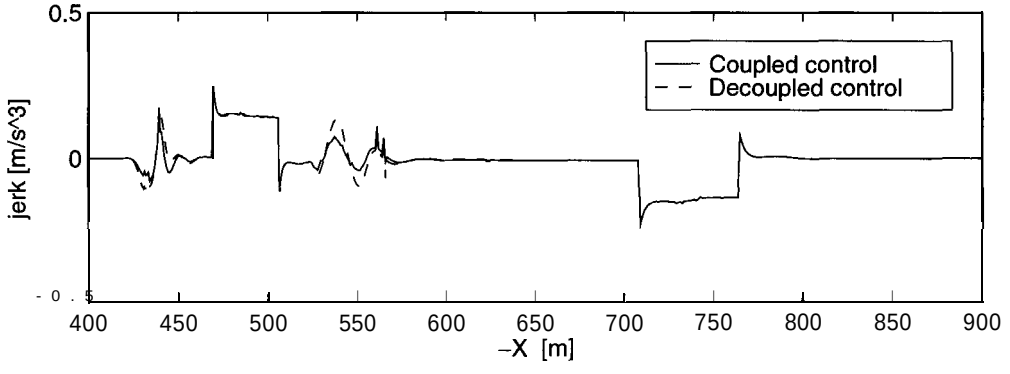

A different test profile is used to demonstrate the effects of high traction demands on lateral cornering performance (Fig 5.5). The profile consists of a severe acceleration ($\dot{V}_{lead} = 1.8\ m/s^2$) beginning at X = 460m. The velocity is ramped from 18m/s (41mph) to 29m/s (65mph). The curve of radius, $\rho = 440m$, represents a maximum lateral acceleration of 1.3 m/s^2. Thus profile II is a mild acceleration/high cornering maneuver, whereas profile I is a high acceleration/mild cornering maneuver.

Figure 5.5. Commanded velocity and road curvature, II.

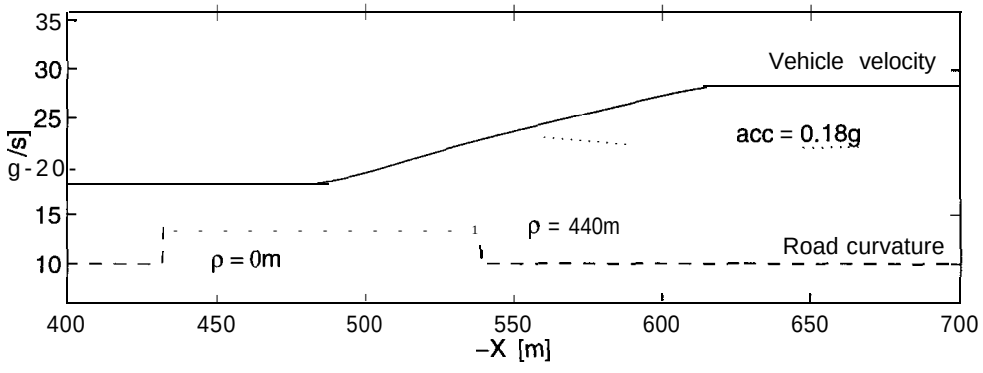

The steering inputs are drawn in Fig 5.6 on the following page. Here, the differences between the coupled and decoupled controls are not as obvious as in the case with throttle. Yet, the lag of the decoupled controller is still noticeable. The lag is most pronounced during the curve exit beginning at X = 540m. The small “dipsy-doodles” (at X = 420m and X = 520m) before curvature changes indicate that the vehicle initiates a lateral maneuver by first turning *away* from the direction of the curve. This results from the curvature shaping filter, and mimics the human driver’s tendency to initially steer away from the turn. It is known that by first turning away, we can finish the turn along a smoother trajectory.

Figure 5.6. Steering inputs of the coupled and decoupled controllers.

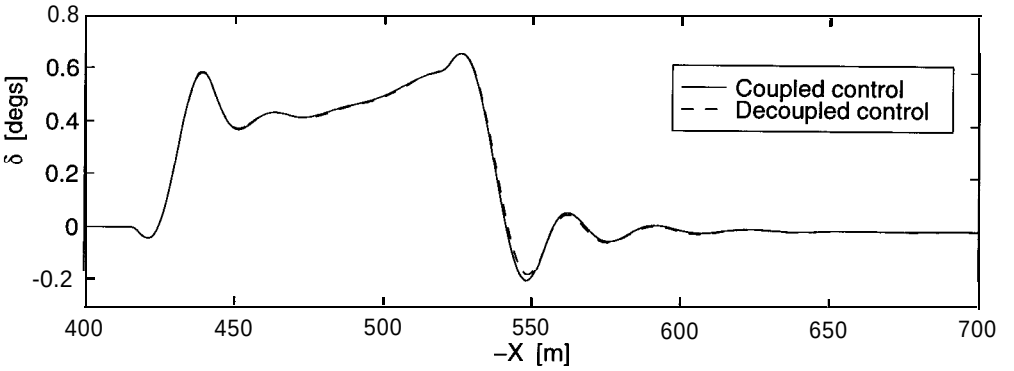

The lateral errors are shown in Fig 5.7 below. The coupled control exhibits consistently tighter tracking over the entire maneuver. Although, this difference is most pronounced during the high longitudinal acceleration section, $X \approx [500\text{m}, 600\text{m}]$.

Figure 5.7. Effect of traction force coupling on lateral tracking performance (Y_s).

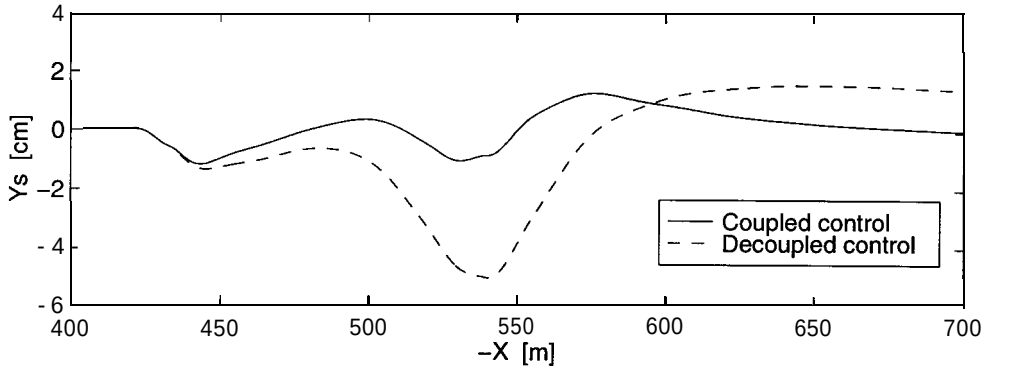

The lateral jerks are shown on the following page in Fig 5.8. Again, the jerks are within the maximum allowable limits. There are no discernible differences ride quality between the coupled or decoupled controls.

Figure 5.8. Lateral ride comfort performance of Sliding controllers.

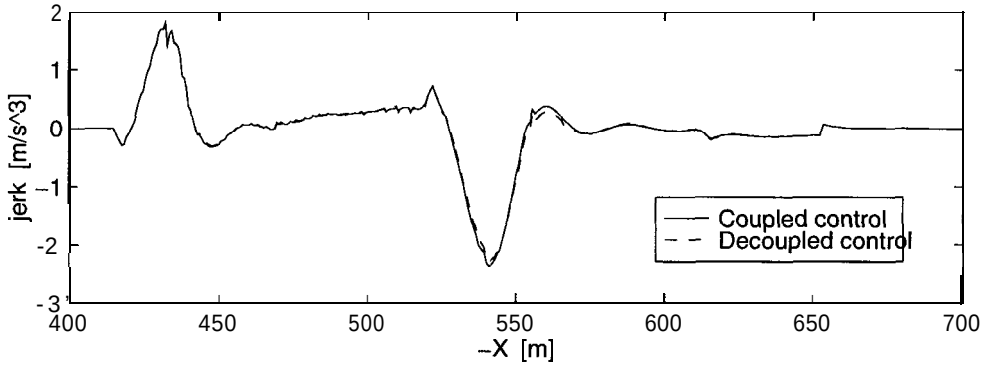

Sliding vs. FSLQ

Having established that the coupling between the lateral and longitudinal tractive forces can affect tracking performance during a combined maneuver, we now present some simulation results comparing the relative performance of linear (FSLQ) and nonlinear (Sliding) controls. The strengths of FSLQ are its nice robustness properties and its providing a systematic approach towards balancing the trade-offs between ride comfort and tracking. The drawbacks include extensive off-line computational demands and inconsistent performance over the entire vehicle operating range. In order to illustrate this point, we contrast the lateral tracking performance of the FSLQ and coupled Sliding controllers under: 1) constant velocity maneuver, 2) quickly varying velocity maneuver.

Figures 5.9a,b on the following page compares the lateral errors, Y,, of the two controls. In the constant velocity maneuver (Fig 5.9a) the curve radius is mild, ρ = 1040m, and the commanded velocity is 22m/s (50mph). This represents a maximum lateral acceleration of $0.5 m/s^2$. In the variable velocity maneuver, the speed is ramped from 22m/s to 36m/s (80mph). The road curvature remains the same. From the figures,

note that the lateral error of the Sliding control remains about the same in both cases. The error for the FSLQ control, however, doubles in the variable velocity case.

Figure 5.9a. Lateral error, Y_s, in constant velocity maneuver, $V_x = 22$m/s.

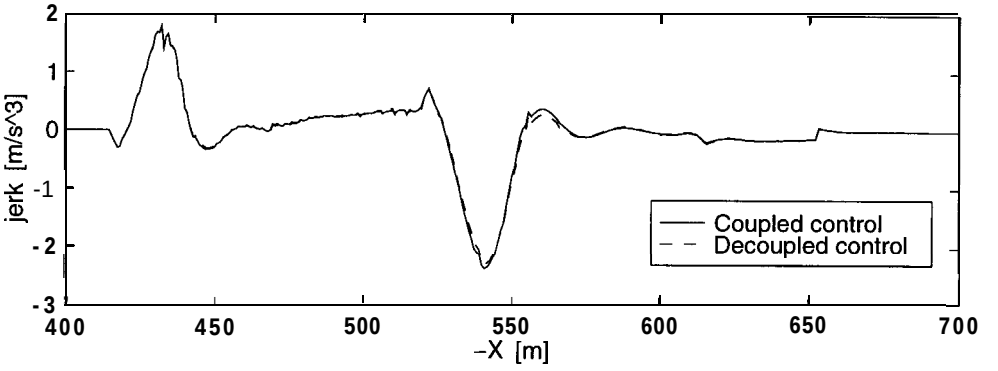

Figure 5.9b. Lateral error, Y_s, in variable velocity maneuver, $V_x = [22\text{m/s}, 36\text{m/s}]$.

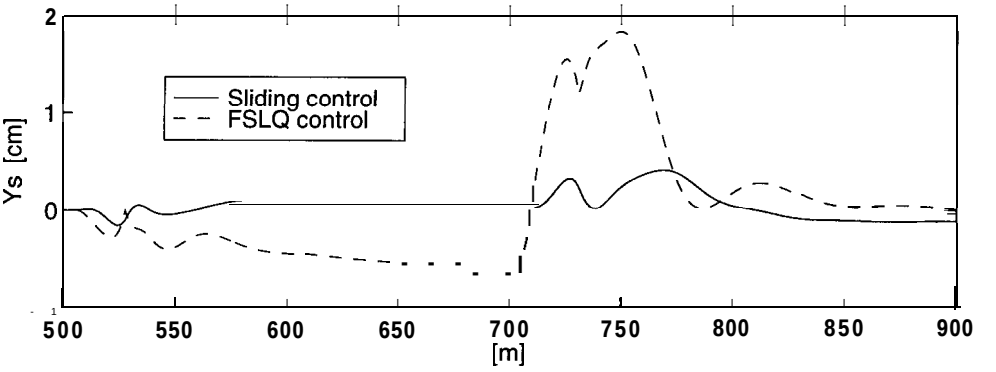

5.2 *Robust performance*

Another important measure of control design is robust performance. In other words, does the controller remain stable despite parametric uncertainties (nominal robustness), and will the tracking error increase appreciably with departures from nominal parameter values or under unknown disturbances (robust performance)? Simulations are

conducted with the coupled Sliding control law to quantify its robustness. Its performance under errors in mass and cornering stiffness estimates and under wind disturbances are compared against the nominal case in the following set of plots.

mass error

The total mass of the vehicle includes passengers and any additional static loads, and hence, is not constant. We can, however, place bounds on the amount the true vehicle weight can deviate from the nominal value. Typically, we expect a range of ±30%. Shown below are simulation results with -20% and -30% mass errors. The same velocity and road profiles as in Fig 5.1 are utilized. Figure 5.10a shows the longitudinal spacing errors (E), and Fig 5.10b shows the lateral errors (Y_s) under erroneous estimates of mass.

Figure 5.10a. Longitudinal robustness against mass estimation errors.

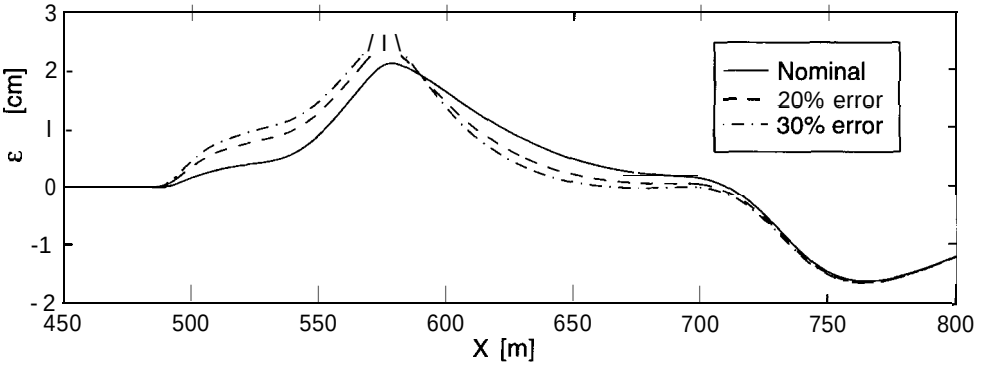

From Fig 5.10a, it is seen that errors in the mass estimates have minimal effect on the longitudinal tracking performance of the Sliding controller. The relative increase in the maximum error is less than 10% for a mass error of 30%. The effect on lateral tracking, conversely, is significantly larger (Fig 5.10b). The lateral error increases by seven-fold in the 30% error case.

Figure 5.10b. Lateral robustness against mass estimation errors.

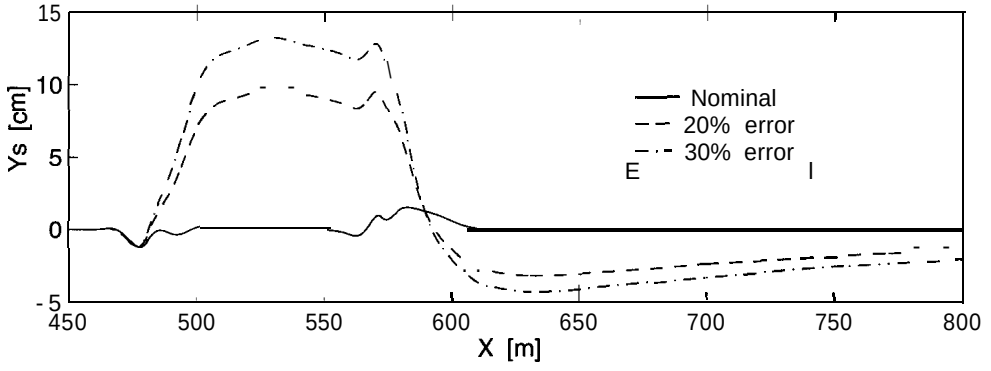

Cornering stiffness error

Like the mass parameter, the cornering stiffness also suffers from large uncertainties. Extraneous factors such as tire pressure, age, temperature, pavement and payload all effect the tire's cornering capabilities. These sundry variables make it impossible to obtain an accurate estimate of the cornering stiffness off-line. Hence, robustness against C_s estimation errors is especially desirable. Errors of 20% and 30% in the cornering stiffness estimates are considered below.

Figure 5.11. Lateral robustness against C_s estimation errors.

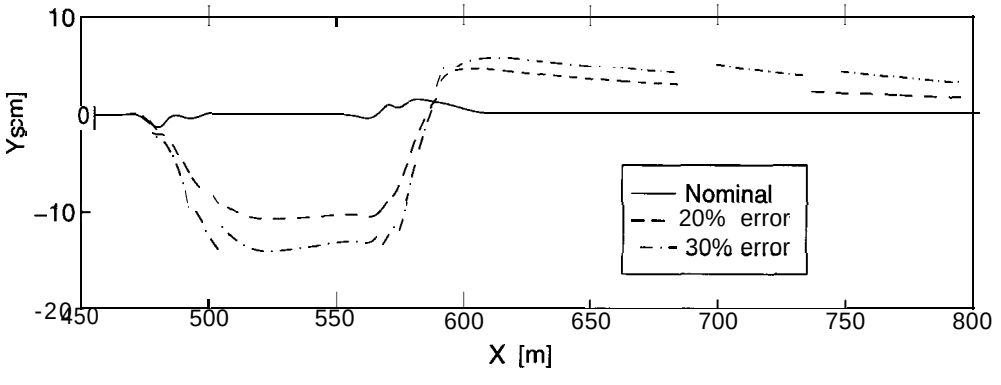

It is seen (Fig 5.11) that the lateral performance is very sensitive to cornering stiffness. The maximum y_s in the case of $+30\%\hat{C}_s$ error is almost 18cm. This represents the outer limits of the magnetometer sensing range and is a cause for concern. This problem may be overcome by adapting on the value of $\hat{C}_s$.

Another approach is to introduce a switching term in the control. Recall that in the controller derivation, a linear attraction term ,ηS, was utilized to guarantee the sliding condition (S=O) in the absence of uncertainties. However, when uncertainties are introduced, the linear term can no longer guarantee the attraction of the surface, S=O. On the other hand, it is well known that a switching term, ηsign(S), can still guarantee surface attraction as long as the magnitude of η is greater than the size of the model uncertainties. Unfortunately, chattering problems associated with discrete-time implementation render the switching solution impractical. Much effort has been devoted to eliminating the chattering problem in literature. Some of these include saturation function/boundary layer control [16], equivalent control [18], and robust observer/controller pair [2]. Some of these results could be tailored to the combined vehicle control problem in the future.

Wind gusts

Finally, wind gusts are added to gauge the Sliding controller's disturbance rejection capability. Figure 5.12a shows the effects of a frontal 20m/s (45mph) wind gust on longitudinal tracking. The 1 second gust begins at X = 540m. The effects of a side wind gust on lateral performance is shown in Fig 5.12b.

Figure 5.12a. Effects of front wind gust on longitudinal error.

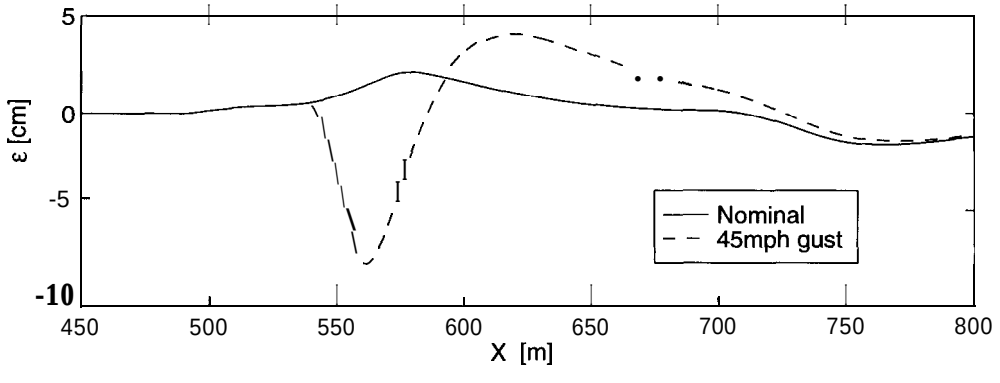

Figure 5.12b. Effects of side wind gust on lateral error.

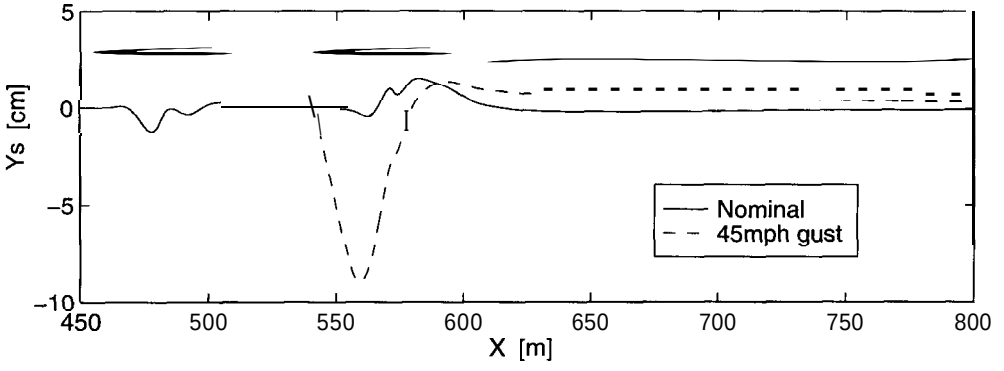

The longitudinal error, ε, is seen to peak at 8cm, while the maximum lateral error, is 9cm. Considering the how rarely wind gusts will exceed 45 mph during normal freeway conditions, these errors are very acceptable. It is concluded, therefore, that the Sliding control provides adequate robustness against unknown wind disturbances.

Moreover, this robustness margin stands to improve with the introduction of some form of the switching control discussed in the previous section on $\hat{C}_s$ cornering stiffness estimation errors.

6. Conclusion

An 18-state vehicle chassis, engine and drive train model was developed and validated against existing longitudinal-only and lateral-only vehicle models. The full-state model was simplified to a 3-state model in order to facilitate controller synthesis. The method of Sliding Mode was taken towards controller design. Two forms of the control law were derived based on the reduced order model. One version was decoupled in the longitudinal and lateral dynamics and forces, while the other retained the coupling terms. Nominal stability of the surface controllers was shown.

To increase ride quality, a l-state lateral error observer with curvature preview information was utilized in the control. The advanced curvature information was used to generate a smooth, “favorable” desired lateral trajectory which maximized the trade-offs between lateral jerk and tracking error. The favorability of this trajectory was determined through extensive simulations.

The Sliding controllers were validated in closed-loop simulations with the complete vehicle model, and comparisons were drawn against the lateral FSLQ controller. Under moderate to severe maneuvers (as measured by the longitudinal and lateral accelerations), the coupling in the tractive forces were significant. In these maneuvers, the coupled form of the Sliding controller exhibited superior tracking. The Sliding controller demonstrated similar performance to the FSLQ's in constant velocity maneuvers. Moreover, the level of the Sliding control’s performance remained constant under rapidly changing velocities, whereas the FSLQ control’s performance was seen to degrade. The robust performance of the Sliding control with the linear surface attraction term was slightly disappointing. It was robust to wind disturbances, but lateral performance degraded under errors in mass and cornering stiffness estimates.

Future work

The surface controller' sensitivity to parameter errors points to a possible need for adaptation. The problem of mass adaptation has been investigated by Swaroop [17]. The variations of C_s are of two types. One type arises from the coupling between the cornering and traction forces. This type of variation is quickly time-varying and can be substantial, according to the severity of the combined lateral and longitudinal maneuver. The other type is due to tire or environmental conditions. These types are more slowly time-varying, but are generally larger. Depending on loads and weather conditions, the variations can exceed 100%. The challenge of a successful adaptation scheme is to distinguish between the two types of variations and to correctly adapt on the desired value.

Or, perhaps a robust control approach could be taken towards the problem of cornering stiffness sensitivity. In this case, some form of a switching control could be introduced.

Another area that needs investigation is the incorporation of brakes into the combined control law. Presently, the simplified model is unable to accommodate the braking effects because it assumes that the speeds across the torque converter are matched. Under heavy braking and unlocked torque converter operation, this assumption can be grossly violated. Consequently, the control model needs to be expanded to include this effect. Also, the present simulation model assumes that the brakes are first-order. This is an extreme oversimplification. A more accurate brake model can be included in the simulation model in order to validate the braking control laws.

The analytical and numerical work to date was undertaken with the goal of eventual implementation in the PATH test vehicles. At this juncture, the bulk of the analytical work has been accomplished, and only some minor fine-tuning remains before preliminary low speed field evaluations can begin. Validation of the longitudinal part of the combined control is facilitated by the fact that it is very similar to the spacing control

law currently implemented by Hedrick et. al. [8]. The lateral validation will take more work since there are, as yet, no field-functioning lateral Sliding controllers. The performance of the FSLQ controller will provide the yardstick for measuring the success and practicality of the lateral part of the combined Sliding control.

Appendix A. Vehicle model parameters

variable	*description*		*value*	
I_x	moment of inertia about x-axis		479.6	[kg-m^2]
I_y	moment of inertia about y-axis		2549.3	[kg-m^2]
I_z	moment of inertia about z-axis		2782.1	[kg-m^2]
J_{eng}	engine inertia		0.2630	[kg-m^2]
$J_{gear}(i)$	i^{th} gear inertia	(1)	0.07582	[kg-m^2]
		(2)	0.08202	
		(3)	0.11388	
		(4)	0.13150	
J_w	wheel inertia		1.2825	[kg-m^2]
m	vehicle mass		1573	[kg]
h_0	vertical distance to c.g		0.487	[m]
h_2	vertical distance from c.g. to roll center		0.30	[m]
h_4	vertical distance from c.g. to pitch center		0.25	[m]
h_5	long. distance from c.g. to pitch center		0.10	[m]
l_1	distance from c.g. to front axle		1.034	[m]
l_2	distance from c.g. to rear axle		1.491	[m]
s_b	track of vehicle		1.450	[m]
r_w	wheel radius		.3044	[m]
C_{s_f}	cornering stiffness of front tire		66366	[N]
C_{s_r}	cornering stiffness of rear tire		52812	[N]
F_{roll}	total tire rolling resistance		274.7	[N]
MAX	maximum manifold intake airflow		684.109	
T_{man}	manifold temperature		310.93	[C^o]
V_{man}	manifold volume		0.00447	[L]
C_x	wind drag coefficient x-dir		.45	
C_y	wind drag coefficient y-dir		2.1	
$r_{gear}(i)$	i^{th} gear ratio	(1)	0.4167	
		(2)	0.6817	
		(3)	1 .0000	
		(4)	1.4993	

Appendix B. Simplified Vehicle Model (SVM) derivation

In this appendix, the simplified vehicle model used for control design is derived from the full simulation model. All assumptions are stated. To reiterate, the vehicle model is expressed by the following state equations.

(B1) $$m[\dot{V}_x - V_y\dot{\psi} + h_4\ddot{\theta} + h_2\dot{\phi}\dot{\psi} + h_2\phi\ddot{\psi}] = \sum_{i=1}^{4} F_{A_i} - C_x V_x^2 - F_{roll}$$

(B2) $$m[\dot{V}_y + V_x\dot{\psi} - h_2\ddot{\phi} + h_4\dot{\theta}\dot{\psi} + h_4\theta\ddot{\psi}] = \sum_{i=1}^{4} F_{B_i} - C_y V_y^2$$

(B3) $$m[\dot{V}_z + V_x\dot{\chi}\beta - h_5\ddot{\theta}] = \sum_{i=1}^{4} F_{P_i} - mg$$

(B4) $$I,\ [\ddot{\phi} - \theta\ddot{\psi} - \dot{\theta}\dot{\psi}] - (I_y - I_z)\dot{\theta}\dot{\psi} = M_x - \theta M_z$$

(B5) $$I_y[\ddot{\theta} + \phi\ddot{\psi} + \dot{\phi}\dot{\psi}] - (I_z - I_x)\dot{\phi}\dot{\psi} = M_y + \phi M_z$$

(B6) $$I_z[\ddot{\psi} + \theta\ddot{\phi} - \dot{\theta}\phi] - (I_x - I_y)\dot{\theta}\dot{\phi} = M_z + \theta M_x - \phi M_y$$

(B7) $$J_{w_i}\dot{\omega}_{w_i} = \frac{1}{2}T_{shaft} - \frac{3}{10}T_{brake} - r_{w_i}F_{x_i} \qquad i = 1, 2 \text{ (front)}$$

$$J_{w_i}\dot{\omega}_{w_i} = -\frac{1}{5}T_{brake} - r_{w_i}F_{x_i} \qquad i = 3, 4 \text{ (rear)}$$

(B8) $$\dot{\omega}_{eng} = \frac{1}{J_{eng}}[T_{eng} - T_{pump}]$$

(B9) $$\dot{m}_{air} = \dot{m}_{air\ in} - \dot{m}_{air\ out}$$

(B10) $$\dot{\alpha} = \frac{1}{\tau_{throt}}[\alpha_C - \alpha]$$

(B11) $$\dot{T}_{brake} = \frac{1}{\tau_{brake}}[T_{brk\,C} - T_{brake}]$$

(B12) $$\dot{\delta}_f = \frac{1}{\tau_{steer}}[\delta_C - \delta_f]$$

By neglecting actuator and manifold dynamics and the roll (q), pitch (f), and vertical (z) motions, the model can be reduced to:

(B13) $$m[\dot{V}_x - V_y\dot{\psi}] = \sum_{i=1}^{4} F_{A_i} - C_x V_x^2 - F_{roll}$$

(B14) $$m[\dot{V}_y + V_x\dot{\psi}] = \sum_{i=1}^{4} F_{B_i} - C_y V_y^2$$

(B15) $$I_z\ddot{\psi} = M_z$$

(B16) $$J_{w_i}\dot{\omega}_{w_i} = \frac{1}{2}T_{shaft} - \frac{3}{10}T_{brake} - r_{w_i}F_{x_i} \qquad i = 1, 2 \text{ (front)}$$

$$J_{w_i}\dot{\omega}_{w_i} = -\frac{1}{5}T_{brake} - r_{w_i}F_{x_i} \qquad i = 3, 4 \text{ (rear)}$$

(B17) $$\dot{\omega}_{eng} = \frac{1}{J_{eng}}[T_{eng} - T_{pump}]$$

The x-moment about the unsprung mass, M_x, can be expressed as:

(B18) $$M_z = l_1(F_{B_1} + F_{B_2}) - l_2(F_{B_3} + F_{B_4}) - \frac{s_{b1}}{2}(F_{A_1} - F_{A_2}) - \frac{s_{b2}}{2}(F_{A_3} - F_{A_4})$$

Under the bicycle model assumption *(i.e.* the dynamics of the left and right side of the vehicle are identical), the moment expression becomes:

(B19) $$M_z = 2l_1(F_{B_f}) - 2l_2(F_{B_r})$$

The external forces are:

(B20) $$\sum_{i=1}^{4} F_{A_i} = 2(F_{x_f} - \delta_f F_{y_f}) + 2F_{x_r} \qquad (\delta_r = 0)$$

(B21) $$\sum_{i=1}^{4} F_{B_i} = 2(F_{y_f} - \delta_f F_{x_f}) + 2F_{y_r}$$

where,

$$F_{x_f} = F_{x_1} = F_{x_2}, \text{ etc.}$$

Noting that the following is true:

$$\begin{aligned} & F_{y_f} - \delta_f F_{x_f} = C_{s_f}(\delta_f - \zeta_f) - \delta_f F_{x_f} \\ \Rightarrow \quad & = \delta_f (C_{s_f} - F_{x_f}) - C_{s_f}\zeta_f \\ \Rightarrow \quad & \approx C_{s_f}\delta_f - C_{s_f}\zeta_f = F_{y_f} \qquad (C_{s_f} >> F_{x_f}) \end{aligned}$$

the lateral forces can be rewritten as:

$$\text{(B22)} \qquad \sum_{i=1}^{4} F_{B_i} \approx 2F_{y_f} + 2F_{y_r}$$

Further, by assuming that $\dot{\omega}_{w_f} = \dot{\omega}_{w_r}$, The simplified state equations (B13-17) is reduced to:

$$\text{(B23)} \qquad \dot{V}_x = -\frac{1}{m}[C_x V_x^2 + F_{roll} - mV_y\dot{\psi} - 2(F_{x_f} + F_{x_r}) - 2\delta_f F_{y_f}]$$

$$\text{(B24)} \qquad \dot{V}_y = -\frac{1}{m}[C_y V_y^2 - mV_x\dot{\psi} - 2(F_{y_f} + F_{y_r})]$$

$$\text{(B25)} \qquad \ddot{\psi} = \frac{2}{I_z}[l_1 F_{y_f} - l_2 F_{y_r}]$$

$$\text{(B26)} \qquad \dot{\omega}_w = \frac{1}{4J_w}[T_{shaft} - T_{brake} - 2r_w(F_{x_f} + F_{x_f})]$$

$$\text{(B27)} \qquad \dot{\omega}_{eng} = \frac{1}{J_{eng}}[T_{eng} - T_{pump}]$$

The engine and brake torques, T_{eng} and T_{brake}, can be related to the traction forces by assuming that the torque converter is locked. In other words, we assume:

i) $\omega_{eng} \approx \dfrac{\omega_w}{r^*}$

ii) $T_{pump} \approx r^* T_{shaft}$

where $r^* = r_{drive} r_{gear}$ is the effective gear ratio.

Under this assumption, the engine and wheel accelerations (B26-27) can be combined to yield:

$$\text{(a)} \quad \dot{\omega}_{eng} = \frac{1}{J_{eng}}[T_{eng} - r^* T_{shaft}]$$

$$\Rightarrow \quad T_{shaft} = \frac{1}{r^*}[T_{eng} - J_{eng}\dot{\omega}_{eng}]$$

$$\Rightarrow \quad T_{shaft} = \frac{1}{r^*}[T_{eng} - J_{eng}\frac{\dot{\omega}_w}{r^*}]$$

$$\text{(b)} \quad \dot{\omega}_w = \frac{1}{4J_w}[T_{shaft} - T_{brake} - r_w F_{x_{tot}}]$$

$$\Rightarrow \quad \dot{\omega}_w = \frac{1}{4J_w}[\frac{1}{r^*}(T_{eng} - J_{eng}\frac{\dot{\omega}_w}{r^*}) - T_{brake} - r_w F_{x_{tot}}]$$

$$\Rightarrow \quad \dot{\omega}_w[J_{eng} + 4J_w r^{*2}] = [r^* T_{eng} - r^{*2} T_{brake} - r_w r^{*2} F_{x_{tot}}]$$

Solving for $F_{x_{tot}}$ and substituting this into eq B23 yields:

$$F_{x_{tot}} = \frac{1}{r_w r^{*2}}[r^* T_{eng} - r^{*2} T_{brake} - \dot{\omega}_w(J_{eng} + 4J_w r^{*2})]$$

$$\Rightarrow \quad \dot{V}_x[1 + \frac{1}{mr_w^2 r^{*2}}(J_{eng} + 4J_w r^{*2})] = -\frac{1}{m}[C_x V_x^2 + F_{roll} - mV_y\dot{\psi} - \frac{1}{r_w r^*}(T_{eng} - r^* T_{brake}) + \delta_f F_{y_f}]$$

define:

$$J^* = mr_w^2 r^{*2} + J_{eng} + 4J_w r^{*2}$$

$$T_{tot} = T_{eng} - r^* T_{brake}$$

The final form of the state equations of the simplified vehicle model is now:

$$\text{(B28)} \quad \dot{V}_x = -\frac{(r_w r^*)^2}{J^*}[C_x V_x^2 + F_{roll} - mV_y\dot{\psi}] + \frac{(r_w r^*)^2}{J^*}[\frac{1}{r_w r^*} T_{tot} + \delta_f F_{y_f}]$$

$$\text{(B29)} \quad \dot{V}_y = -\frac{1}{m}[C_y V_y^2 - mV_x\dot{\psi} - 2(F_{y_f} + F_{y_r})]$$

$$\text{(B30)} \quad \ddot{\psi} = \frac{2}{I_z}[l_1 F_{y_f} - l_2 F_{y_r}]$$

Appendix C. Tire model (Bakker-Pacjeka)
Fitted on Yokohoma P205/60R1487H steel-belted radials

(C1) $$F_x = D_x \sin(C_x \tan^{-1}(B_x\phi_x)) + S_{vx}$$

(C2) $$F_y = D_y \sin(C_y \tan^{-1}(B_y\phi_y)) + S_{vy}$$

(C3) $$\phi_x = (1 - E_x)(i_s + S_{hx}) + \frac{E_x}{B_x} \tan^{-1}(B_x(i_s + S_{hx}))$$

(C4) $$\phi_y = (1 - E_y)(\nu + S_{hy}) + \frac{E_y}{B_y} \tan^{-1}(B_y(\nu + S_{hy}))$$

traction ($i_s > 0$)

$$B_x = 22 + \frac{F_z - 1940}{645}$$

$$C_x = 1.35 - \frac{F_z - 1940}{16125}$$

$$D_x = 1750 + \frac{F_z - 1940}{.956}$$

$$E_x = -3.6$$

$$S_{hx} = 0$$

$$S_{vx} = 0$$

braking ($i_s < 0$)

$$B_x = 22 + \frac{F_z - 1940}{430}$$

$$C_x = 1.35 - \frac{F_z - 1940}{16125}$$

$$D_x = 1750 + \frac{F_z - 1940}{.956}$$

$$E_x = 0.1$$

$$S_{hx} = 0$$

$$S_{vx} = 0$$

$$B_y = 0\,22 + \frac{5200 - F_z}{40000}$$

$$C_y = 1.26 + \frac{F_z - 5200}{32750}$$

$$D_y = -0.00003F_z^2 + 1.0096F_z - 22.73$$

$$E_x = -1.6$$

$$S_{hy} = 0$$

$$S_{vy} = 0$$

References

[1] Bakker, E., Pacejka, H. B., Lidner, L. "A New Tire Model with an Application in Vehicle Dynamics Studies," *SAE Transactions, Journal of Passenger Cars,* Vol. 98, 1989, SAE Technical Paper No. 890087.

[2] Bartolini, G., Pydynowski, P. "Chattering Phenomenon in VSC of Uncertain Nonlinear Systems: The Use of Time Varying Observers," *Proceedings of the 32nd Conference on Decision and Control,* San Antonio, TX, 1993.

[3] Cho, D., Hedrick, J. K. "Automotive Powertrain Modeling for Control," *Transactions ASME Journal of Dynamic Systems, Measurement and Control,* Vol. 111, No. 4, Dec. 1989.

[4] Fernandez, B., Hedrick, J. K. "Control of Multivariable Nonlinear Systems by the Sliding Mode," *International Journal of Control*, Vol. 46, Sept. 1987, pp. 1019-1040.

[5] Gerdes, C., Maciuca, D., Devlin, P., Hedrick, J. K. "Brake System Modeling for IVHS Longitudinal Control," ASME WAM, *Advances in Robust and Nonlinear Control Systems,* DSC-Vol. 53, 1993, pp. 119-126.

[6] Godthelp, H. "Vehicle Control During Curve Driving," *Human Factors,* 28(2), 1986, pp. 211-221.

[7] Green, J., Hedrick, J. K. "Nonlinear Torque Control for Gasoline Engines," *Proceedings of the 1990 American Control Conference,* San Diego, CA, 1990.

[8] Hedrick, J. K., McMahon, D., Narendran, V., Swaroop, D. "Longitudinal Vehicle Controller Design for IVHS Systems," *Proceedings of the 1990 American Control Conference,* San Diego, CA, 1990.

[9] McMahon, D. H., Hedrick, J. K., Shladover, S. E. "Vehicle Modeling and Control for Automated Highway Systems," *Proceedings of the 1991 American Control Conference,* 1991, pp. 3107-3112.

[10] Moskwa, J. J., Hedrick, J. K. "Modeling and Validation of Automotive Engines for Control Algorithm Development," ASME WAM, *Advanced Automotive Technologies,* DSC-Vol. 13, 1989, Ed. Karmel, A. M. et al.

[11] Peng, H. "Vehicle Lateral Control for Highway Automation," Ph.D. dissertation, UC Berkeley, 1992.

[12] Peng, H., Tomizuka, M. "New Tire Model for the Toyota Celica Test Vehicle," PATH internal report, Apr. 1991.

[13] Peng, H., Tomizuka, M. "Lateral Control of Front-Wheel-Steering Rubber-Tire Vehicles," University of California, Berkeley: Institute of Transportation Studies, California PATH Program, UCB-ITS-PRR-90-5, Jul. 1990.

[14] Sakai, H. "Theoretical and Experimental Studies on the Dynamical Properties of Tyres, Part 4: Investigations of the Influences of Running Conditions by Calculation and Experiment," *International Journal of Vehicle Design,* Vol. 3, 1982, pp. 333-375.

[15] Shladover, S. E. "Program on Advanced Technology for the Highway (PATH)," *Road Transport Znformatics (RTI)/Intelligent Vehicle-Highway Systems (ZVHS),* 24th International Symposium on Automotive Technology and Automation, Florence, Italy, 199 1.

[16] Slotine, J.-J. E., Li, W. *Applied Nonlinear Control,* Englewood Cliffs, N.J.: Prentice-Hall Inc., 1990.

[17] Swaroop, D. "String Stability of Interconnected Systems: An Application to Platooning in Automated Highway Systems," Ph.D. dissertation, UC Berkeley, 1994.

[18] Utkin, V. I., "Sliding mode control in discrete-time and difference systems," in *Variable Structure and Lyapunov Control,* pp.83-103, London, U.K.: Springer-Verlag, 1993.

[19] Wong, J. *Y. Theory of Ground Vehicles,* New York: John Wiley & Sons, 1978.